Analysis of Low-Energy Lunar Transfers in a High-Fidelity Dynamics Model

Patrick J. Torchia

Thesis submitted to the Faculty of the
Virginia Polytechnic Institute and State University
in partial fulfillment of the requirements for the degree of

Master of Science
in
Aerospace Engineering

Riley M. Fitzgerald, Chair
Shane D. Ross
Kevin K. Schroeder

May 10, 2023
Blacksburg, Virginia

Keywords: STK, NASA GRAIL, Low-Energy Lunar Transfer, High-Fidelity, Simulation

Analysis of Low-Energy Lunar Transfers in a High-Fidelity Dynamics Model

Patrick J. Torchia

(ABSTRACT)

Renewed interest in returning to the Moon, emboldened by recent directives and missions by NASA, has necessitated the establishment of lunar infrastructure to support continuous human presence. With that, the objective of making this return more cost effective has gained significant importance. Low energy lunar transfers are more efficient ways to reach the Moon than the traditional Hohmann-type transfer. These trajectories leverage the multi-body gravitational effects to reduce overall Δv requirements, in some cases removing the capture Δv completely. While the time of flight for these transfers can be much longer than a Hohmann-type transfer, the chaotic design space of these transfers can enable large changes in arrival conditions at the Moon for small changes in initial conditions. Many investigations of these transfers take place in simplified dynamical models, such as the Planar Circular Restricted Three Body Problem, with very few higher-fidelity models being implemented. This approach is good to understand the dynamics of these trajectories as well as provide initial guesses for higher-fidelity models; but approximating the dynamics heavily make these models less applicable to mission design. This thesis aims to investigate the application of a higher-order model to simulate these trajectories. STK Astrogator was used to recreate the NASA GRAIL trajectory; and from the recreated trajectory, a nominal trajectory absent of mid-course corrections was established. This nominal trajectory was used to perform parametric and variational studies of departure and arrival conditions as well as compare to a nominal trajectory in a reduced-fidelity model. An investigation into the post launch

correction burn requirements following launch vehicle under-performance was completed. Utilizing low energy transfers proved beneficial to adjusting arrival conditions for low Δv requirements. All arrival inclinations are reasonably achievable for around 255 m/s. Using 255 m/s as a baseline, right ascension of the ascending node could be reached in a 40° range and argument of periapsis in a 50° range. Lunar insertion arrival can be varied by 7 hours on either side for less than 80 m/s. Trans-lunar injection epoch can be varied by 7 hours on either side of nominal departure for less than 4 m/s. Orbit radius and initial velocity are the most expensive errors to correct. These trajectories can be tuned to reduce the overall mid-course correction Δv requirement for differing arrival inclinations if other orbital elements are relaxed. A relationship between placement of post-launch correction maneuver for velocity or radius errors was found. Comparing the trajectory in STK to the Inclined Bi-Elliptic Restricted Four Body problem, revealed that timing of the trajectory is variable while keeping the same arrival and departure conditions. However, solar radiation pressure cannot be ignored for more accurate simulation of these trajectories. This investigation has shown that low energy lunar transfers are a viable method to reach the Moon and their chaotic nature can be leveraged to relax restrictions in the design space.

Analysis of Low-Energy Lunar Transfers in a High-Fidelity Dynamics Model

Patrick J. Torchia

(GENERAL AUDIENCE ABSTRACT)

Returning to the Moon has become a more important goal within the space industry. This has required more cost-efficient ways to reach the Moon; an important cost savings being fuel. Traditional ways to reach the Moon required large amounts of fuel to be expended to remain around the Moon after launch. Low energy lunar transfers aim to reduce fuel usage while still reaching the Moon, although they take much longer to reach their destination. Fuel and energy have direct comparisons and are used to evaluate these transfers. These transfers are highly susceptible to changes in their trajectory making them ideal for transferring to the Moon in different orientations. These changes can be made using very little fuel, allowing for more resources to be brought to the Moon. Navigating these transfers to the Moon require an accurate model of space for mission design.

Dedication

To my parents, Cindy and Jason Torchia, for allowing me the freedom to grow and explore, and supporting me in my endeavors.

Acknowledgments

Thank you to Dr. Riley Fitzgerald, my faculty advisor. The guidance and support over countless hours of work on this research is invaluable. Without you, this thesis would not have been realized.

Thank you to my committee for providing instruction and knowledge on the basis for this work. Dr. Kevin Schroeder has provided me with a deeper understanding of modeling and simulation in this field. Dr. Shane Ross has done expansive work in this subject has provided a treasure trove of information to refer to. It is truly a benefit to have someone who can say they wrote the textbook.

Thank you to the faculty and staff of the Kevin T. Crofton Aerospace Engineering Department and Virginia Polytechnic Institute and State University. This research would not have been possible without the resources and instruction provided.

Thank you to the friends I have made throughout my time in Blacksburg; without you I would probably go insane.

Contents

List of Figures

List of Tables

List of Abbreviations

β	Launch Azimuth Angle
Δv	change in velocity
γ_{H}	Horizontal Flight Path Angle
$\hat{r}_s$	position vector of the sun as seen from the spacecraft
$\mathcal{E}$	Specific Orbital Energy
$\mathrm{C_r}$	Coefficient of Reflectivity
$\mathrm{C_3}$	Launch Energy
$\mathrm{DEC_{AV}}$	Declination of the Apoapsis Vector
DEC	Declination
$\mathrm{H_P}$	Altitude of Periapsis
$\mathrm{R_{mag}}$	Magnitude of Orbit Radius from the Center of the Earth
$\mathrm{V_{Azimuth}}$	Initial Velocity Azimuth Angle
$\mathrm{V_{mag}}$	Initial Velocity Magnitude
μ	standard gravitational parameter
ν_{M}	True Anomaly at the Moon
Ω_{E}	Right Ascension of the Ascending Node at Earth

Ω_{M} Right Ascension of the Ascending Node at the Moon

ω_{M} Argument of Periapsis at the Moon

Ω_{AV} Right Ascension of the Apoapsis Vector

ϕ launch site latitude

ϕ solar flux at 1 AU

A Area of the spacecraft

c speed of light

e eccentricity

i Inclination

K percentage of the Sun as seen from the spacecraft that is not eclipsed

m Mass of the spacecraft

R_{AU} position from the spacecraft from the Sun in AU

AU Astronomical Unit

BBR Body-Body Rotating

CAPSTONE Cislunar Autonomous Positioning System Technology Operations and Navigation Experiment

EGM Earth Gravitational Model

ERTBP Elliptic Restricted Three Body Problem

ESA European Space Agency

GRAIL Gravity Recovery and Interior Laboratory

HPOP High-Precision Orbit Propagator

IBERFBP Inclined Bi-Elliptical Restricted Four-Body Problem

ICRF International Celestial Reference Frame

JPDLE or DE Jet Propulsion Laboratory Development Ephemeris

KPLO Korean Pathfinder Lunar Orbiter

LGAS Lunar Get Away Special

LOI Lunar Orbit Insertion

MCS Mission Control Sequence

NASA National Aeronautics and Space Administration

PCRTBP Planar Circular Restricted Three-Body Problem

SMART-1 Small Missions for Advanced Research in Technology-1

STK Systems Toolkit

TLI Trans-Lunar Injection

TOF time-of-flight

UTCG Gregorian Coordinated Universal Time

VNC Velocity Normal Conormal

WSB Weak Stability Boundary

Chapter 1

Introduction

With the lively beginning of the Space Age, particularly between 1950-1970, increased activity to reach and study the Moon was seen. Following the ending of the Apollo program, lunar missions fell into a lull with the last crewed mission to the Moon just over 50 years ago. With renewed interest in returning to the Moon, spurred on by NASA's Artemis program and the planned establishment of a Lunar Gateway, and the necessity of establishing infrastructure for a continuous human presence, the objective of returning to the Moon for lower cost has become a higher priority. A large contributor to the cost of reaching the Moon is the fuel requirements of the spacecraft. Requiring more fuel to reach the Moon reduces the overall payload that can be brought along.

The two common transfers to reach the Moon are the Hohmann transfer and free-return trajectories. A Hohmann transfer is built within the two-body model utilizing a Keplerian ellipse. This ellipse has a periapsis at Earth and an apoapsis at the Moon, resulting in a new periapsis at the Moon. This transfer is hyperbolic in nature and therefore requires the hyperbolic excess velocity to be removed at the Moon to complete capture. While this transfer has a short time of flight (3 days), the fuel cost associated with this would be prohibitive for missions with lower available fuel resources. Free-return trajectories also exist within the two-body framework. These trajectories leverage the gravitational interaction of the Moon to return a trajectory back to Earth with no additional propulsion. While these trajectories had relevance in the Apollo missions, a trajectory that returns without

additional propulsion would be beneficial to return human astronauts should components of the mission fail, missions that do not require to return from the Moon or consider a human component could be better served with a different transfer type. Free-return trajectories also approach the Moon with hyperbolic geometry, requiring large fuel costs to lower perilune and capture at the Moon. For missions with lower propulsion requirements than would allow for a Hohmann transfer or do not require return to the Earth could be better served by low energy lunar transfers.

Low energy lunar transfers are a class of transfers that rely heavily on the concept of ballistic capture. Ballistic capture leverages multi-body gravitational effects, these will be known as the Weak Stability Boundary (WSB) or invariant manifolds, within the Sun-Earth-Moon system to naturally reduce Keplerian energy with respect to the Moon [18]. Ballistic transfers achieve capture around the Moon without propulsion requirements outside of the initial launch requirements. While capture may be unstable, resulting in the spacecraft leaving the vicinity of the Moon, these trajectories can be fully captured utilizing propulsive maneuvers. These transfers approach the Moon with elliptical geometry (relative to the Moon) and the required capture maneuvers have been found to be cheaper than a Hohmann transfer equivalent, thus making them low energy, as demonstrated by Belbruno and Miller [4], Yagasaki [35], and Sousa-Silva et al. [30]; although, resulting in much longer times of flight. Given that these transfers utilize multi-body gravitational effects, the two-body model is not sufficient to realize the dynamics of these transfers. At the minimum, a three-body model must be implemented [1, 3, 8, 10, 12, 15, 16, 18, 20, 27, 29, 30].

Low energy lunar transfers can be classified into two types given the shape drawn out by the trajectory. Interior low energy lunar transfers exhibit a spiral from the Earth that gradually raises the apoapsis of the orbit until it reaches the orbit of the Moon. These transfers have been used in applications for low thrust missions such as the proposed Lunar Get Away

Special (LGAS) [23] and the European Space Agency (ESA) Small Missions for Advanced Research in Technology-1 (SMART-1) [22]. The SMART-1 mission one mission employed low thrust propulsion to execute a slow spiral from its orbit around Earth to get captured at the Moon [22]. Exterior transfers are characterized by trajectories that proceed beyond the orbit of the Moon, notably Earth-Sun Lagrange points, before returning within the orbit of the Moon. Applications of exterior transfers have been seen in Hiten, NASA Gravity Recovery and Interior Laboratory (GRAIL) , Cislunar Autonomous Positioning System Technology Operations and Navigation Experiment (CAPSTONE) , and the Korea Pathfinder Lunar Orbiter (KPLO) [4, 11, 14, 32]. The Hiten mission used an exterior transfer to capture ballistically at the Moon following propulsion constraints during the mission [4]. The GRAIL mission used an exterior transfer with 2 mid-course correction maneuvers and an insertion burn to perform a low-energy lunar transfer [28]. The CAPSTONE mission followed a ballistic capture trajectory to the Moon that eventually resulted in a Near Rectilinear Halo Orbit at the Moon [32]. The KPLO mission followed a similar trajectory to the GRAIL mission although performed its insertion burn at a different point along the orbit of the Moon [14].

The main benefit to low energy lunar transfers is a reduction in propulsion requirements, specifically arrival Δv, in some cases even capturing ballistically. These fuel savings allow for smaller and cheaper missions to the Moon to be realized as well as more mass to be allocated to payload instead of propulsion. These transfers can extend the launch window as seen in the trajectory design of GRAIL and KPLO [14, 17]. The chaotic design space of these transfers can be seen as a double-edged sword to mission design. In terms of trajectory design, small adjustments in initial conditions may result in significant changes to arrival conditions, easing restrictions on launch conditions. Although, due to the sensitive nature of these trajectories, tracking and orbit determination requirements may be higher to perform

these adjustments. For urgent or human missions, the time-of-flight (TOF) of these transfers may not be viable, as these transfers at a minimum will take 70 days [25], but for missions where expediency is not a main priority, these transfers could ease restrictions on other mission parameters.

Many studies into the dynamics of low energy lunar transfers have been done in simplified models. The Planar Circular Restricted Three-Body Problem (PCRTBP) is often used to investigate creation of these trajectories [1, 3, 8, 15, 18, 27, 29] and investigate the geometry of celestial bodies [3, 18, 29]. While this model provides a good basis to understand the dynamics of these transfers, their use in mission design is limited. Solutions created within the three-body model can be used as initial guesses for higher fidelity models as seen in works by Koon et al. [15] and Luo and Topputo [18]. Methods to further capture the natural dynamics not encapsulated in the PCRTBP are to relax the restrictions within the three-body model. These include creating a spatial three-body model (including motion in a third dimension), Gómez et al. [10], Masdemont [20], or accounting for the elliptical nature of the orbits of the Earth and Moon (thus creating an Elliptic Restricted Three Body Problem (ERTBP)), Hyeraci and Topputo [12], Topputo and Belbruno [33] . A further expansion is to generate trajectories within a higher N-body model, such as the four-body model. The four-body model can either be decomposed into two patched three-body models as seen in works by Koon et al. [15] and Sousa-Silva et al. [30] or full trajectories integrated within the model as seen in works by Belbruno and Miller [4], Fitzgerald [6], Romagnoli and Circi [27], Topputo [34], Yagasaki [35], and Scheuerle Jr. [29]. As with three-body models, four-body models can contain varying degrees of restriction, the most common being the Bicircular Model, which assumes planar and circular orbits of all bodies. Further expansion of the four-body model would be increasing it to a spatial model, Belbruno and Miller [4], Romagnoli and Circi [27]. The most accurate modelling of space dynamics involves utilizing celestial ephemeris data to

determine position of celestial bodies. Ephemerides contain a list of positions and velocities of celestial bodies numerically integrated throughout equally spaced intervals of time in a common frame of reference, such as the International Celestial Reference Frame (ICRF) . The NASA Jet Propulsion Laboratory Development Ephemeris (JPLDE or DE) is a commonly used model for planetary ephemerides; these models are updated frequently to include new masses, relativistic effects, and perturbations from celestial bodies for increased accuracy to fit "real life" measurements, Park et al. [24]. These models present numerically integrated solutions to a large-scale N-body problem. Few investigations into low energy lunar transfers utilize celestial ephemerides [4, 18, 19, 25]. In addition to providing more accurate positions for calculation of gravitational forces, other orbital perturbations can be included, such as, planetoid oblateness (e.g. Earth J2-J4 perturbations), higher-fidelity gravity models (i.e. expanding the point-mass approximation to spherical harmonic models), and solar radiation pressure.

As computing power increases, the numerical simulation of these trajectories becomes quicker and easier. With this increase, higher fidelity models for gravitational bodies can be used as well as other orbital perturbations (e.g., eccentricity, inclination, oblateness, solar radiation pressure) can be accounted for. This thesis aims to use Systems Toolkit (STK) , a modern astrodynamics software, to study low energy lunar transfers in higher fidelity, using ephemeris models and accurate propagators. Specifically, exterior low energy lunar transfers will be the focus of this investigation. The NASA GRAIL mission will be recreated in STK following published information and insights into modeling low-energy lunar transfers in this environment will be presented. Following, sensitivity studies in orbit parameters at the Moon and Earth on a nominal trajectory, placement of the first corrective maneuver post launch, and an investigation into launch requirements for a "zero maneuver" trajectory will be presented. Comparison of the nominal trajectory within a reduced-fidelity model will

be conducted.

Chapter 1 of this thesis encompassed a short introduction to low energy transfers and their benefits as a transfer. Chapter 2 will provide a background into the methods for creating and studying low energy transfers and the capabilities of STK. Chapter 3 will detail methods for recreating a low energy lunar transfer in STK and the set-up for the following investigations. Chapter 4 will present the results and discuss connections to previous work. Chapter 5 will conclude this thesis.

Chapter 2

Background and Models

In this chapter, background on constructing the planar circular restricted three-body problem and two methods for creating preliminary low-energy trajectories will be introduced. Within that, notable dynamics within the three-body model are presented. At the end, the capabilities of STK that are employed within the simulation of these trajectories are outlined.

2.1 Three-Body Problem

The general three-body problem aims to solve the motion of three bodies using Newton's Laws of Motion and Newton's Law of Universal Gravitation. There is no analytical solution to the three-body problem, and it is highly chaotic. In order to simplify analysis of this problem, certain restrictions can be applied; such as assuming that the masses of two bodies are much larger than the mass of the third ($m_1 > m_2 \gg m_3$) and that the third body does not gravitationally affect the other two masses, the two large masses complete circular orbits around a mutual barycenter, and the motion of the three bodies is restricted to two dimensions (thus keeping the bodies within a plane). These assumptions create the Planar Circular Restricted Three-Body Problem (PCRTBP), a common starting point for understanding the dynamics of the Earth-Moon system and Sun-Earth system, with a spacecraft being considered as the less-massive third body.

2.1.1 Equations of Motion

The non-dimensional equations of motion for the PCRTBP in a counterclockwise rotating frame are given in Equations 2.1 - 2.3 following the derivation by Szebehely [31],

$$\ddot{x} - 2\dot{y} = \Omega_x \tag{2.1}$$

$$\ddot{y} + 2\dot{x} = \Omega_y \tag{2.2}$$

$$\Omega = \frac{(x^2 + y^2)}{2} + \frac{1-\mu}{r_1} + \frac{\mu}{r_2} \tag{2.3}$$

where

$$r_1^2 = (x-\mu)^2 + y^2 \tag{2.4}$$

$$r_2^2 = (x+1-\mu)^2 + y^2 \tag{2.5}$$

and the subscript x and y representing the partial derivative with r_1, r_2 representing the distance of the spacecraft from the first and second primaries (i.e. Sun and Earth or Earth and Moon). Ω represents the effective potential in the rotating frame and writing Ω explicitly in terms of the rotating PCRTBP x, y coordinate system yield Equation 2.6.

$$\Omega = \frac{x^2 + y^2}{2} + \frac{1-\mu}{\sqrt{(x-\mu)^2 + y^2}} + \frac{\mu}{\sqrt{(x+1-\mu)^2 + y^2}} \tag{2.6}$$

μ is a mass parameter of the system such that $m_2 = \mu$ and $m_1 = 1 - \mu$, in normalized mass units, or more generally $\mu = m_2/(m_1 + m_2)$. The origin of the system rests at the center of mass with Primary 1 and Primary 2 placed along the x-axis such that $(x, y)_2 = (1 - \mu, 0)$

and $(x, y)_1 = (-\mu, 0)$. Figure 2.1 shows the PCRTBP coordinate system and the placement of the primaries as applied to the Sun-Earth system.

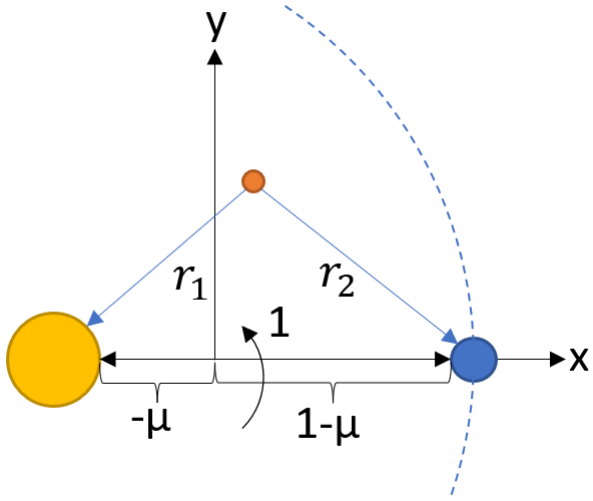

Figure 2.1: Normalized synodic coordinate frame of the PCRTBP, illustrated for the Sun-Earth system

These equations of motion can be rewritten in terms of the Hamiltonian, E, given by Equation 2.7 [15].

$$\mathrm{E} = \frac{1}{2}(\dot{x}^2 + \dot{y}^2) - \Omega(x, y) \tag{2.7}$$

This can be related the Jacobi constant, $\mathrm{C_J}$, a conserved quantity within the circular restricted three-body problem, by Equation 2.8.

$$\mathrm{C_J} = -2\mathrm{E} \tag{2.8}$$

The Jacobi constant defines accessible regions of a spacecraft within the influence of two gravitational bodies via the zero-velocity curves. In a sense, the Jacobi constant serves as an

analogue to the two-body specific orbital energy, $\mathcal{E} = -\frac{\mu}{2a}$, which limits orbit size. Figure 2.2 displays the accessible regions for example values of the Jacobi constant for a system with mass parameter $\mu = 0.0123$. As more energy is given to the spacecraft, these curves open up between the two massive bodies, allowing for transit between them. As seen in Figure 2.2c and Figure 2.2b the accessible regions do not open up symmetrically, instead a small neck region forms between the two bodies connecting the accessible regions before another opens as an exit outside of the system on the other side of the smaller body. This necking phenomenon is what allows low-energy transfers with ballistic capture to be possible.

2.1.2 Lagrange Points

The three-body problem has five equilibrium points, know as Lagrange points; three of which lie along the line connecting the two bodies ($L_1 - L_3$), and two which complete equilateral triangles between the two bodies (L_4 and L_5). In the normalized coordinate system, the triangular Lagrange points can be found geometrically, the coordinate pair being described as $(x, y) = (0.5 - \mu, \pm\frac{\sqrt{3}}{2})$. The collinear Lagrange points can be found by assuming that all accelerations and velocities are zero. This creates Equations 2.9 and 2.10.

$$0 = \Omega_x = x - \frac{\mu(x - 1 + \mu)}{\sqrt{((x - 1 + \mu)^2 + y^2)^3}} - \frac{(1 - \mu)(x - \mu)}{\sqrt{((x + \mu)^2 + y^2)^3}} \tag{2.9}$$

$$0 = \Omega_y = y - \frac{\mu y}{\sqrt{((x - 1 + \mu)^2 + y^2)^3}} + \frac{y(1 - \mu)}{\sqrt{((x + \mu)^2 + y^2)^3}} \tag{2.10}$$

By inspection, Equation 2.10 is still satisfied if $y = 0$, leaving Equation 2.9 to provide the location for the collinear Lagrange points. Solution of this equation must be done numerically as no analytical form of the solution exists. Another version of the equations of motion give a

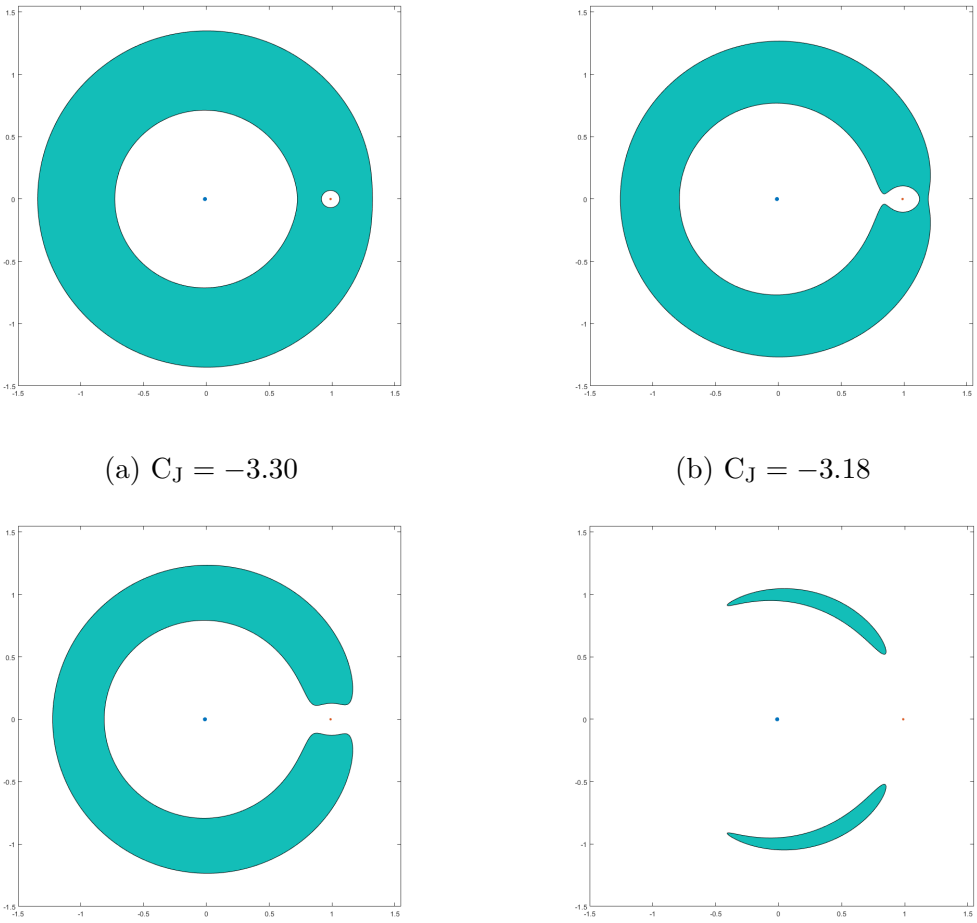

(a) $C_J = -3.30$ (b) $C_J = -3.18$

(c) $C_J = -3.14$ (d) $C_J = -3.00$

Figure 2.2: Accessible (white) and inaccessible (teal) regions in the PCRTBP for various values of C_J, for a system with $\mu = 0.0123$

quintic polynomial with roots that describe the locations, this too has no analytical solution. Figure 2.3 presents the three-body model with the five Lagrange points. Figure 2.4 shows a contours of Jacobi Energy, showing how the Lagrange Points affect the contours with increasing energy.

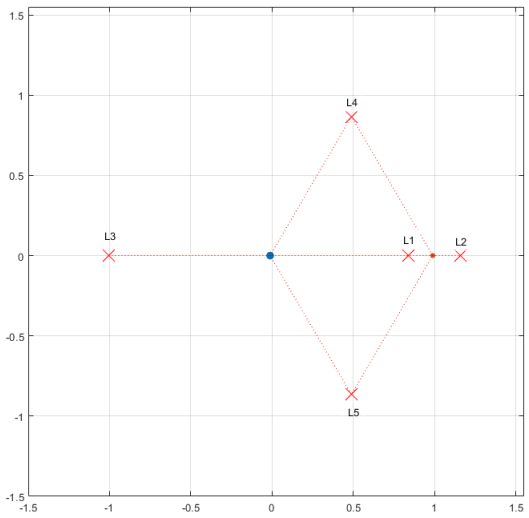

Figure 2.3: Locations of the Lagrange points for $\mu = 0.0123$

2.1.3 Regimes of Motion around Lagrange Points

In the seminal work by Conley [5] in 1968, the motion of orbits around Lagrange points are broken into four regimes. The first is the unstable but periodic Lyapunov orbit, this orbit can be grown into a larger family of orbits given proper initial conditions. The second are asymptotic orbits; these orbits can wind on to or off of the periodic Lyapunov orbit. Drawing multiple asymptotic orbits on either side of the Lyapunov orbit will generate tubes that are known as invariant manifolds (to be discussed in Section 2.2). The third are transit orbits. These orbits allow spacecraft to travel through connecting regions between celestial bodies, a useful dynamic for low energy transfers. The fourth are non-transit orbits which

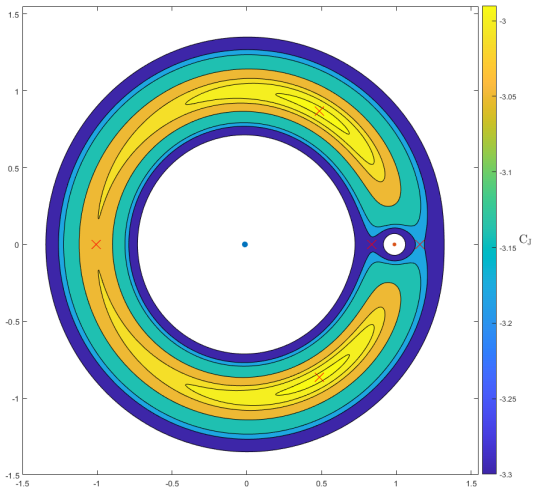

Figure 2.4: Locations of the Lagrange for various values of C_J, for a system with $\mu = 0.0123$

will approach the transit region of the Lyapunov orbit but will not pass through, instead turning around. Figure 2.5 depicts the four orbital regimes outlined by Conley.

2.2 Invariant Manifolds and Weak Stability Boundary

With the basic dynamics of the PCRTBP explained, it can be leveraged to create low-energy lunar transfers. There are two approaches to creating these trajectories, invariant manifold patching and weak stability boundary theory. As mentioned in Section 2.1.3, invariant manifolds are created by the collection of orbits that exhibit asymptotic behavior to the periodic solution, creating a tube structure in phase space separating the transit and non-transit orbits. Manifolds are separatrices of the regimes of motion around a Lagrange point [15]; orbits that exist inside the manifolds are transit orbits, orbits that exist on the manifolds are asymptotic orbits, and orbits that exist outside of these orbits are non-transit orbits. There are four invariant manifolds that connect to one periodic solution,

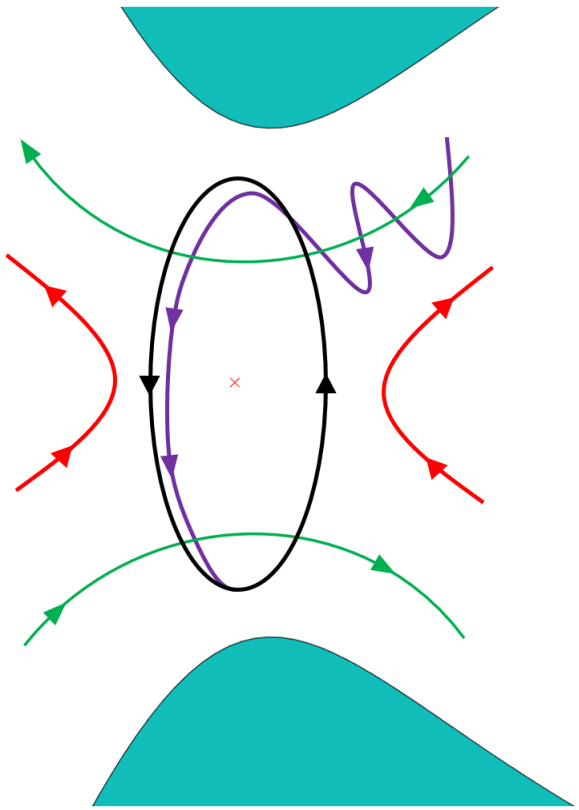

Figure 2.5: A qualitative depiction of the four orbital regimes described by Conley [5], showing periodic (black), asymptotic (purple), transit (green), and non-transit orbits (red).

two on either side. These invariant manifolds are defined by two types, unstable manifolds and stable manifolds; unstable manifolds prescribe orbits that fall away from the periodic solution and stable manifolds contain orbits that "jump onto" the periodic solution.

Because these trajectories typically target the Earth-Sun L_1, a four-body model is preferred. The four-body is an expansion of the three-body problem, adding in another massive body; for the purposes of low-energy lunar transfer, this would be the Sun (creating a Sun-Earth-Moon-Spacecraft model). A common method to analyze the four-body problem is to patch together two three-body problems (thus creating a Sun-Earth-Spacecraft model and a Earth-Moon-Spacecraft model). The deconstruction assumes that one of the three massive bodies has negligible effect on the spacecraft compared to the other two massive bodies. The concept of manifold patching, in the context of low energy lunar transfers, aims to utilize a collection of stable and unstable manifolds to create a trajectory within the three-body system. This is similar to the two-body concept of patched conics. These manifolds are easily found in the planar three-body problem, but they also exist and act as separatrices within the spatial three-body problem [10]. The itinerary for a typical low energy lunar transfer is:

- A non-transit trajectory outside the manifold tubes of the Earth-Sun L_1
  - Approach L_1 nearby a stable manifold
  - Leave L_1 nearby an unstable manifold
- A transit trajectory inside the manifold tube of the Earth-Moon L_2
  - Approach L_2 inside a stable manifold tube

To begin patching manifolds, a stable manifold is generated from the Earth-Sun L_1 point in backwards time, towards the Earth. A cut is made transverse to the manifold, typically intersecting the Earth for easier targeting, creating a 2D projection in position-velocity space

known as a Poincaré section. The action of making a cut transverse to the manifold allows for position and velocity to be considered in one dimension, typically the y dimension, as the cut is along the same x position and the velocity in the x direction is the nature of the trajectory. The y direction is chosen to satisfy the desired orbit radius from the Earth and be enclosed within the projection to allow the trajectory to transit between regions. Following this, an unstable manifold from the Earth-Sun L_1 point in forward time and a stable manifold from the Earth-Moon L2 point in backward time are propagated until intersecting the Poincare cut made along the Earth. With this, the projections of each of these manifolds can be compared and a point chosen along the Poincare section to satisfy transit orbit through the stable manifold and non-transit orbit on the unstable manifold. The solution that this method creates can be used as an initial guess within higher fidelity models [15].

Another method to generate low energy lunar transfers is Weak Stability Boundary theory. The Weak Stability Boundary (WSB) is defined within the three-body problem as the region where the gravitational forces between bodies acting on a mass m tend to cancel out. This concept was introduced by Edward Belbruno in 1987 [1] for the Lunar GAS mission [23], as a region where the perturbations from the Moon could lead to a trajectory capturing around the Moon. Determining the weak stability boundary around the Moon is done by choosing a point of interest to become the capture point with desirable orbital elements around the Moon and connecting a line from the Moon to that point of interest; this line will also draw a plane of reference. From there an initial velocity is given at the capture point in the direction of approach. The trajectory of the point is then propagated forward in time until it crosses the plane of reference. The relative lunar orbital elements for the trajectory and deviations from the capture point are measured. Placing the capture point further away from the moon will eventually yield a point where the eccentricity becomes greater than or equal to 1. The point where the eccentricity is equal to 1 can be considered the weak stability boundary,

at this point perturbations from the Moon can lead to capture. As this point is unstable, choosing a point with eccentricity less than 1 will yield an orbit that will remain captured around the Moon for a longer period. This is typically described as the stability number, n [3]. To determine a proper departure point at the Earth, the initial condition given at the capture point can be propagated backwards until a desired point near the Earth is reached [1]. While this method originally applied to an interior type transfer, it is also applicable to exterior type transfers. Both methods have been found to overlap with each other under certain circumstances [3], but invariant manifolds require more robust definitions around the periodic solutions that exist within the model utilized for study. Weak Stability Boundary is heuristically defined and therefore contains a more general definition that can be present in higher fidelity models. Manifold patching does allow for easier creation of trajectories as conditions at patch points can be fine-tuned; whereas weak stability boundary is found through grid search.

2.3 Higher-Fidelity Models

While these simpler models can aid in transfer construction and provide insight into the dynamical structure of the Sun-Earth-Moon system, higher-fidelity models are required for real mission design. An intermediate step to higher-fidelity models is to use ephemeris point-mass models to describe the motion of the massive bodies. Using ephemerides no longer constrains the bodies to planar circular motion. Further, modeling the gravitational field of the massive bodies using spherical harmonic models provides more accurate force modeling than point mass approximations. This thesis aims to use as high-fidelity a propagator as is available, such as STK Astrogator.

The Astrogator propagator allows for high-fidelity orbit propagation and mission design.

Central body objects within STK utilize a default ephemeris; in STK 12.5, this ephemeris is the JPL DE430 [7]. Using Mission Control Sequence (MCS), the satellite object ephemeris can be built in pieces. Tied into the MCS are two targeting methods for meeting mission goals, the differential corrector and an optimizer. The differential corrector profile allows for changes in control variables to meet defined equality conditions. An optimizer can be used to adjust control parameters to best meet a goal within a set of constraints. Astrogator has several built-in numerical propagators to model forces acting upon a satellite object. The default propagators utilized in this study are the Earth HPOP Default v10 and the Moon HPOP Default v10. The Earth HPOP Default v10 uses propagator functions for gravitational forces from the Earth, Sun, and Moon, the Jacchia-Roberts Atmospheric Density Model, and a spherical solar radiation pressure model. The Earth gravitational force function uses the EGM2008 gravity field model, by default this is set to degree and order 21. Both the Moon and Sun gravitational forces are modeled as point masses. The numerical integrator used in the propagator is a 7th order Runge-Kutta-Fehlberg integrator with 8th order error control and variable step size. The Moon HPOP Default v10 propagator uses propagator functions for Moon, Earth, and Sun gravitational forces and a spherical solar radiation pressure model. The Moon gravitational force is based on the LP150Q gravity model (by default, degree = order = 48), and the Earth and Sun are modeled as point masses. The numerical integrator used the same 7th order Runge-Kutta-Fehlberg method. While these propagators are built into STK, the list of functions and integrator methods is not exhaustive, and STK affords the ability to build custom propagators that can incorporate more propagator functions or different integration methods.

2.3.1 Jacchia-Roberts Atmospheric Model

The Jacchia-Roberts atmospheric model is a reference model for temperature, density, pressure, atmospheric composition, and other properties of the Earth's atmosphere with height from sea level. This model was first introduced in 1965 [13] but was updated until 1977. This model is based on the concept of the static atmosphere and covers altitudes from 90 km to 2500 km. This model uses equations to present values for atmospheric properties throughout the entire range of altitudes that align well with data on spacecraft drag. This model accounts for latitudinal, seasonal, geomagnetic, and solar effects.

2.3.2 EGM2008 Gravity Field Model

The Earth Gravitational Models (EGM) are a series of spherical harmonic models used to approximate the gravitational potential of the Earth, with EGM2008 being the most accurate currently available. The EGM2008 model uses a least squares combination of data from the GRACE mission as well as terrestrial, altimetry-derived, and airborne gravity data. This model is complete up to a degree and order of 2159 [26].

2.3.3 LP150Q Gravity Field Model

Similar to the EGM2008 gravity model, the LP150Q model uses spherical harmonics to fit a model of the Moon's gravitational field to the gravitational field data collected by the Lunar Prospector mission in 1998. This model is complete up to a degree and order of 150 [21].

Chapter 3

Methods and Performed Analysis

In this chapter, the reconstruction of the NASA GRAIL mission in an STK simulation will be explored. Following that, a new nominal trajectory that eliminates the midcourse maneuvers performed in the original trajectory will be created. The nominal trajectory will be used as a baseline for parametric studies in arrival and departure conditions. An investigation into first maneuver timing following post launch performance was completed.

3.1 Reconstructing GRAIL in Simulation

The baseline reference for studies of low-energy transfers to low lunar orbit is the NASA GRAIL mission. The initialization of the scenario began by creating a scenario within the timeframe of the NASA GRAIL Mission and setting the Earth as the central body. Three planet objects were created: Earth, Moon, and Sun. A satellite object was created to model the GRAIL trajectory. As the ground track of this trajectory was not important to this study, the 2D graphics window was set to an orthographic projection with a Body-Body Rotating (BBR) coordinate frame with the Sun as the Secondary Body. This created a rotating frame to keep the Earth and Sun stationary, and specifies the top-down view seen in Figures 3.1 - 3.5.

Initial conditions at the Earth and final conditions at the Moon found for the GRAIL mission [11, 28, 36, 37] were used as an initial guess for the differential corrector profile. The initial

conditions at Earth are presented in 3.1.

Table 3.1: GRAIL Earth Literature Values

Elements	Values	Reference
Launch Date	10 September 2011	Zuber et al. [37]
C_3	$-0.693\ \frac{km^2}{s^2}$	Roncoli and Fujii [28]
DEC_{AV}	$-6.164°$	Roncoli and Fujii [28]
Ω_{AV}	$190.548°$	Roncoli and Fujii [28]
β	$93°$	Roncoli and Fujii [28]

Declination and Right Ascension were given with respect to the apoapsis vector of the trajectory. Typical launch declination and right ascension are given with respect to the outgoing hyperbola; because these low energy lunar transfers do not begin on a hyperbolic trajectory, they are defined by the ellipse created. In the two-body problem, this ellipse would complete a full orbit without being perturbed from its trajectory.

Using spherical coordinates, these initial conditions were converted to the following initial guess, Table 3.2. A full state vector or complete set of descriptors was not found, therefore this state is underdetermined and additional information was needed.

Table 3.2: Initial guess for Earth departure spherical elements

Elements	Values	Reference
Epoch	10 September 2011 14:00:00.000 UTCG	Zuber et al. [37]
Ω_E	$10.5776°$	Calculated from Ω_{AV}, [28]
DEC	$6.164°$	Calculated from DEC_{AV}, [28]
R_{mag}	6678 km	Assumed
γ_H	$0°$	Assumed
$V_{Azimuth}$	$62.0236°$	Calculated from β, [28]
V_{mag}	$10.8942\ \frac{km}{s}$	Calculated from R_{mag} and C_3, [28]

To assist in determining the full state, the initial conditions were modeled to represent a trans-lunar injection burn at the periapsis of the instantaneous departure ellipse. Declination for the trajectory was assumed to be the same magnitude but with a sign change, right

ascension was found by subtracting 180 from the Ω_{AV}, velocity azimuth was found from determining the launch inclination

$$i = \cos^{-1}(\sin\beta\cos\phi) \tag{3.1}$$

and subtracting the inclination from 90°, where β is the launch azimuth angle and ϕ is the launch site latitude. The latitude used for Cape Canaveral Florida (the launch site) was 28.5904°. The horizontal flight path angle was assumed to be 0°. $\mathrm{R_{mag}}$ was chosen by assuming a 300 km altitude initial orbit and $\mathrm{V_{mag}}$ was found by using the specific orbital energy equation

$$\mathcal{E} = \frac{1}{2}V^2 - \frac{\mu}{R} = \frac{1}{2}\mathrm{C_3} \tag{3.2}$$

where μ is the standard gravitational parameter of Earth.

Running an uncorrected trajectory with these initial conditions demonstrated that the provided $\mathrm{C_3}$ energy appeared to be unable to create the desired trajectory, instead failing to reach the vicinity of the Earth-Sun $\mathrm{L_1}$ Lagrange Point and falling back around the Earth. Figure 3.4 shows this initial guess trajectory.

To correct this, velocity was added until the desired shape was approximately replicated. This resulted in an adjusted $\mathrm{V_{mag}}$ of 10.8958 $\frac{\mathrm{km}}{\mathrm{s}}$ and an adjusted initial $\mathrm{C_3}$ energy of -0.659 $\frac{\mathrm{km}^2}{\mathrm{s}^2}$. This resulted in a 0.0016 $\frac{\mathrm{km}}{\mathrm{s}}$ velocity difference; the error from this could come from failing to account higher-order gravity terms in the initial velocity/energy calculations. The adjusted trajectory using the new initial velocity is shown in Figure 3.2.

The lunar final conditions are given in Table 3.3.

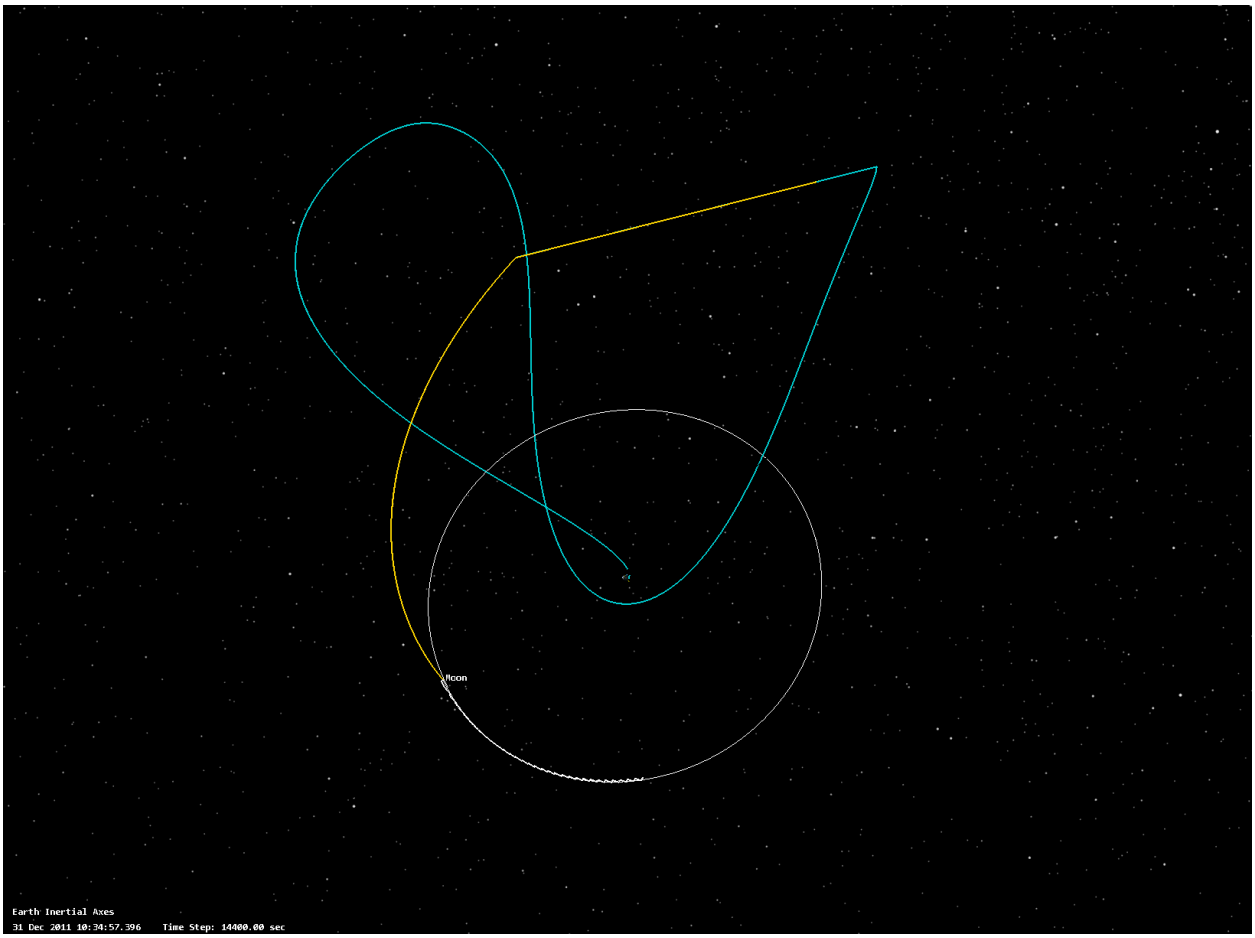

Figure 3.1: Original trajectory utilizing initial velocity guess in the Earth Inertial Frame. The blue trajectory is the forward propagation from Earth and the yellow trajectory is the backward propagation from the Moon. The white orbit is the orbit of the Moon.

Table 3.3: GRAIL Moon Literature Values

Elements	Values	Reference
Arrival Date	31 December 2011	Zuber et al. [37]
H_P	84 km	Roncoli and Fujii [28]
i	88.17°	Hatch et al. [11]

Figure 3.2: Original trajectory utilizing adjusted initial velocity guess in the Earth Inertial Frame. The blue trajectory is the forward propagation from Earth and the yellow trajectory is the backward propagation from the Moon. The white orbit is the orbit of the Moon.

Using Keplerian osculating orbital elements with respect to the Moon, the initial conditions were converted to the full orbital state in Table 3.4.

Table 3.4: Initial guess for Moon arrival Keplerian Elements

Elements	Values	Reference
Epoch	31 December 10:00:00.000 UTCG	Zuber et al. [37]
H_P	84 km	Roncoli and Fujii [28]
e	0.98	Assumed
i	88.17°	Hatch et al. [11]
Ω_M	120°	Assumed
ω_M	0°	Assumed
ν_M	0°	Assumed

It is assumed that the capture burn at the Moon was conducted at perilune, therefore argument of perigee and true anomaly were set to 0°. The eccentricity of the orbit was assumed to be slightly below one as that is the edge of the weak stability boundary [1] corresponding to nearly-parabolic arrival. A Mission Control Sequence (MCS) was created in the Astrogator propagator in STK. An MCS sequence is a series of segments that define the transfer and the mission; these segments can define initial state conditions, input maneuvers, and propagate the state throughout time. This MCS sequence details a patched trajectory that propagates forward in time from the initial departure conditions at Earth, includes the two midcourse correction maneuvers performed by GRAIL-A (the first of the two spacecraft) and patches to a trajectory that is propagated backwards in time from the arrival conditions at the Moon. The sequences contained the correction maneuvers and the circularization burns around the Moon utilized by GRAIL-A. Figure 3.3 presents the structure of the MCS sequence used to simulate GRAIL-A in STK.

The following subsections will describe each step of the Mission Control Sequence corresponding to a different phase of the replicated GRAIL-A trajectory.

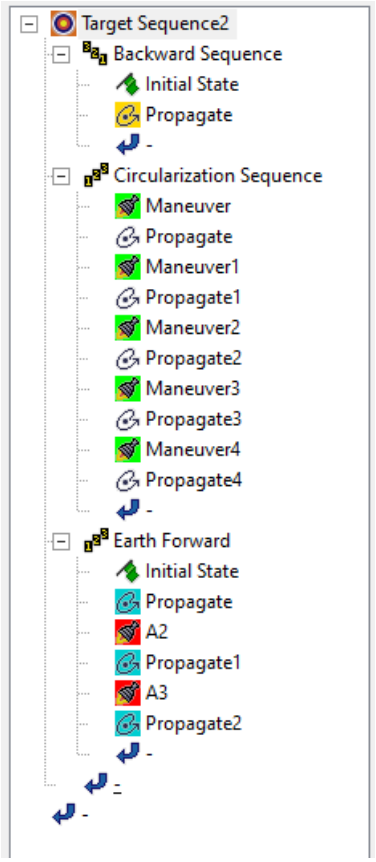

Figure 3.3: Mission Control Sequence Structure for trajectory.

3.1.1 Lunar Backward Sequence

This backward sequence began with an Initial State segment and is followed by a propagate sequence. Backwards sequences in STK uses the Initial State segment to define the end state of the trajectory and integrate in backwards time, thus creating the trajectory before it arrives at the Moon. The end state was defined by its osculating Keplerian orbital elements (see Table 3.4) within the Moon Inertial coordinate system. Epoch, Eccentricity, Right Ascension of the Ascending Node and Argument of Periapsis were specifically stored as independent variables for later differential correction. The spacecraft dry mass was assumed to be 200 kg and fuel tank mass was assumed to be 106 kg [28]. After the initial state sequence, a Propagate sequence was created. This sequence utilized the Moon HPOP (High-Precision Orbit Propagator) Default v10 propagator built in to Astrogator and contained an Epoch stopping condition of 16 Dec 2011 12:00:00.000 UTCG. This stopping condition was arbitrary but provides a consistent epoch between the Moon and Earth to patch the two sequences together. The backward sequence was set to pass the initial state to the next sequence, the lunar circularization sequence.

3.1.2 Lunar Circularization Sequence

This forward sequence contained five Maneuver and five Propagate segments. Each maneuver was be modeled as impulsive, utilized the Moon HPOP Default v10 propagator and had thrust applied along the anti-velocity vector. The magnitude of each maneuver was as follows: 191.7 m/s, 78.7 m/s, 71.2 m/s, 11.7 m/s, and 11.6 m/s. Each propagate segment was placed after each maneuver, utilized the Moon HPOP Default v10 propagator and contained a stopping condition at the periapsis of the Moon. This set up a sequence that included the capture burn and subsequent circularization burns each orbit to bring GRAIL A into

a science orbit. This sequence was added for completeness of the trajectory, but it is not relevant for the goals of this investigation. In subsequent studies, this sequence was shortened to only include the capture burn to expedite calculations.

3.1.3 Earth Forward Sequence

This forward sequence contained the segments from the beginning of the trajectory up to the patch point, including the scheduled midcourse correction maneuvers completed by GRAIL A. The initial state was defined by the spherical elements at the Earth (see Table 3.2), calculated in the Earth J2000 coordinate system. Orbit Epoch, Radius Magnitude, Horizontal Flight Path Angle, Velocity Azimuth, and Velocity Magnitude were set as independent variables for use within the differential corrector. The spacecraft dry mass was assumed to be 200 kg and fuel tank mass was assumed to be 106 kg [28]. The first propagate segment utilized the Earth HPOP Default v10 propagator and contained a Duration stopping condition for 20 days. The first Maneuver segment is placed, modeled as impulsive and using the Earth HPOP Default v10 propagator. The attitude of this maneuver was a thrust vector on the Velocity-Normal-Conormal (VNC) (Earth) axes. A 12.4 $\frac{\text{m}}{\text{s}}$ burn was given along the x (velocity)-axis. The second Propagate segment was set up similar to the first segment with a longer Duration stopping condition at 67 days. The second Maneuver segment was set up similar to the first, applying an 11.48 $\frac{\text{m}}{\text{s}}$ burn along the x-axis. The final Propagate segment used the Earth HPOP Default v10 propagator and contains an Epoch stopping condition at 16 December 2011 12:00:00.000 UTCG, matching the backwards Lunar Segment. For use in the differential corrector, the results at the end of this Propagate segment were created to match position and velocity in three dimensions between the end of the Earth segment and the end of the backwards Lunar Segment, thus creating six equality constraints.

3.1.4 Differential Corrector Profile

A Target Sequence segment was used to patch the forwards and backwards trajectories together. Each sequence was placed inside the Target Sequence segment. A differential corrector profile was used to target the position and velocity differences between segments. The desired value for each position and velocity was 0 m and 0 $\frac{\text{m}}{\text{s}}$, respectively. The tolerances were set to 0.1 m and 0.1 $\frac{\text{m}}{\text{s}}$. The control parameters are: Lunar Epoch, Lunar Eccentricity, Lunar Right Ascension, Lunar Argument of Periapsis, Earth Epoch, Earth Orbital Velocity Azimuth, Earth Horizontal Flight Path Angle, Earth Orbit Radius, and Earth Orbital Velocity. The root-finding algorithm used was Newton-Raphson Method and calculation of derivatives utilized the forward difference method.

3.1.5 Final Converged Conditions:

The converged initial conditions at the Earth are given in Table 3.5.

Table 3.5: Converged elements for Earth departure spherical elements

Elements	Values
Epoch	10 September 2011 10 Sep 2011 14:00:00.000000000 UTCG
Ω_{E}	10.5776°
DEC	6.164°
R_{mag}	6678.081 265 550 279 567 833 1 km
γ_{H}	−0.700 695 384 603 556 958 9°
$\text{V}_{\text{Azimuth}}$	48.457 500 778 092 921 223 1°
V_{mag}	10.895 756 785 004 579 114 7 $\frac{\text{km}}{\text{s}}$

The converged final conditions at the Moon are given in Table 3.6

The precision of these elements were held out to 9 digits for epochs and 19 digits for the remaining elements to avoid truncation errors when propagating the trajectory. Because of the chaotic nature of these trajectories (exacerbated because STK defaults to a variable step

Table 3.6: Converged elements for Moon Keplerian Elements

Elements	Values
Epoch	31 December 31 Dec 2011 10:59:58.971123001 UTCG
H_P	84 km
e	0.9873588220500001400
i	88.17°
Ω_M	129.307 522 466 046 407 316 8°
ω_M	352.271 688 608 430 224 576 3°
ν_M	$9.541\,66 \times 10^{-15}$ deg

size method), truncating digits from initial conditions will lead to large deviations later along the trajectory. The tolerances used to achieve this transfer can be relaxed if convergence is not easily reached but nothing further than 0.5 m for position is recommended. Figure 3.4 displays the converged GRAIL-A trajectory.

Due to the nature of the GRAIL mission, the mid-course correction maneuvers may not be necessary to correct deviations from the original trajectory. The GRAIL mission separated two orbiters to follow each other in their science orbits. To simplify the reference transfer before study, the trajectory was adjusted to remove the mid-course maneuvers. This was done using the same differential corrector profile to find the original trajectory while both maneuvers were manually reduced to $0\,\frac{m}{s}$. Tables 3.7 and 3.8 give the resulting converged Earth departure and Moon arrival conditions, respectively.

Table 3.7: Converged elements for nominal Earth spherical elements

Elements	Values
Epoch	10 September 2011 10 Sep 2011 14:00:00.000001000 UTCG
Ω_E	10.5776°
DEC	6.164°
R_{mag}	6678.226 786 688 515 858 259 1 km
γ_H	0.058 045 985 270 754 746 3°
$V_{Azimuth}$	48.565 825 655 911 623 925 9°
V_{mag}	10.895 859 189 461 722 493 8 $\frac{km}{s}$

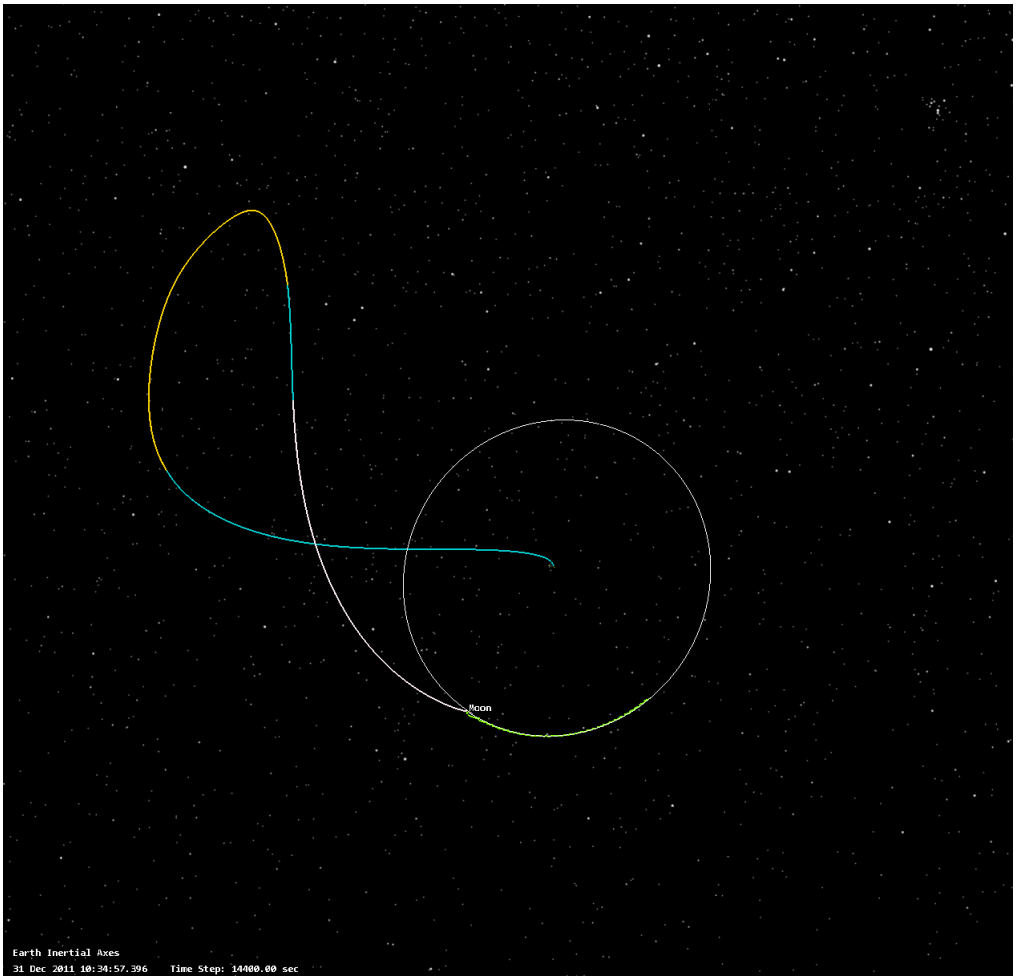

Figure 3.4: Converged original trajectory in the Earth inertial frame. The first blue segment is the post launch trajectory up to the first correction maneuver, the yellow segment is the trajectory between the two correction maneuvers, the second blue segment is the trajectory up to the patch point, the off-white trajectory is from the patch point to the Moon arrival, and the green trajectory is the circularization burn. The white circular orbit is the Moon.

Moon Conditions:

Table 3.8: Converged elements for nominal Moon Keplerian Elements

Elements	Values
Epoch	31 December 31 Dec 2011 10:34:57.395594001 UTCG
H_P	84 km
e	0.9881480983397944451
i	88.17°
Ω_M	133.860 575 778 393 013 024 5°
ω_M	354.807 567 294 875 582 319 9°
ν_M	$7.951\,39 \times 10^{-16}$ deg

This refined trajectory will serve as the nominal trajectory from which the sensitivity studies and other results were conducted. This trajectory was also the nominal trajectory for investigating corrective maneuver placement following less than ideal launch vehicle performance. Figure 3.5 presents both trajectories

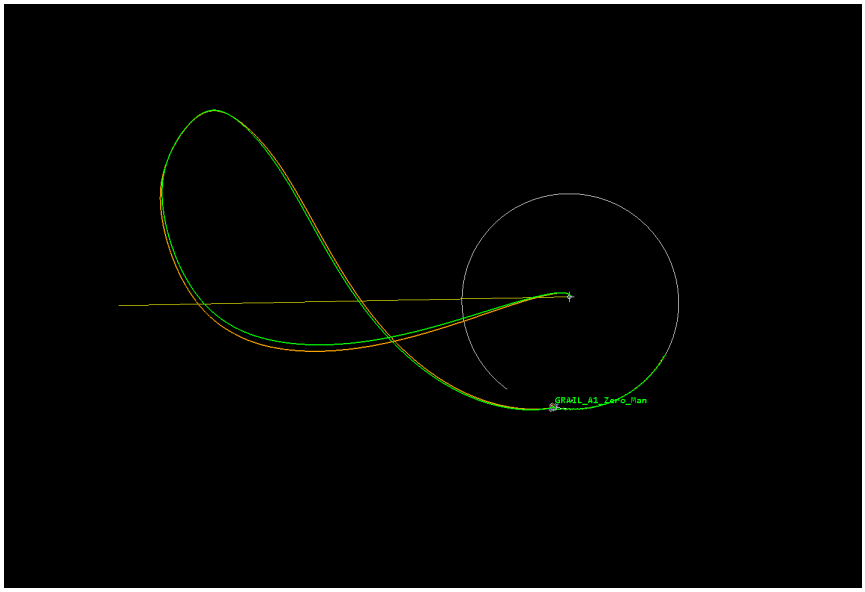

Figure 3.5: Comparison of original trajectory (orange) to nominal trajectory (green). Note the slight differences in the loop in the vicinity of the Earth-Sun L_1 point.

3.2 Parametric and Variational Studies of Departure and Arrival

While the reference trajectory is an acceptable transfer modeled after GRAIL, one may be interested in modifying the arrival or departure conditions. It is worth studying what happens to propulsion requirements should the arrival conditions be changed. In the context of multi-craft missions or ride-share, should the arrival conditions be different between spacecrafts, the instability of low energy lunar transfers could be leveraged to reach those conditions without significant penalties to payload.

Parametric studies on orbital parameters were conducted to determine Δv requirements to adjust the trajectory to reach different arrival conditions. The objective is to vary a single parameter from the reference trajectory and account for the change with the mid-course maneuvers. This represents either correction of launch deviations or change/distributions of arrival conditions. An analyzer profile was set up in STK to vary one orbital element at either the Earth or the Moon. A new differential corrector profile was set up; the control parameters being a 3D thrust vector for both correction maneuvers and the equality constraints being the 3D difference in position and velocity at the patch points with the same tolerances as before. This creates a sequence that varies a single parameter and attempts to adjust the nominal trajectory using the two maneuvers available. The 3D maneuver components and total Δv of each maneuver were collected (the following results will only present the total magnitude of each maneuver).

For the lunar elements, inclination, right ascension, argument of periapsis, and LOI epoch were varied. The range and resolution considered in the variational study are given in Table 3.9.

Table 3.9: Lunar elements for parametric studies

Parameters	Range	Resolution
i	0° - 180°	0.5°
Ω_{M}	0° - 360°	0.5°
ω_{M}	0° - 360°	0.5°
Epoch	± 7 hrs	1 min

For Earth elements, orbit radius, orbital velocity, and TLI epoch were varied. The range and resolution considered in the variational study are given in Table 3.10.

Table 3.10: Earth elements for parametric studies

Parameters	Range	Resolution
$\mathrm{R}_{\mathrm{mag}}$	$6671 - 6700$ km	0.1 km
$\mathrm{V}_{\mathrm{mag}}$	$10.89 - 11 \frac{\mathrm{km}}{\mathrm{s}}$	$0.0005 \frac{\mathrm{km}}{\mathrm{s}}$
Epoch	± 7 hrs	1 min

3.3 Variation of Departure Energy with Arrival Inclination

Equivalent required launch energy for inclination changes were found by utilizing the differential corrector profile similar to the one used to create the nominal trajectory. The launch energy and arrival energy required for a zero-maneuver trajectory are calculated by using two forms of the specific orbital energy equation:

$$\mathcal{E} = \frac{1}{2}V^2 - \frac{\mu}{R} \tag{3.3}$$

$$\mathcal{E} = \frac{\mu(e-1)}{2\mathrm{R}_{\mathrm{p}}} \tag{3.4}$$

The inclination was manually varied from 10° to 110°. Tolerances on equality constraints were set to 0.1 m and 0.1 $\frac{\text{m}}{\text{s}}$. Spherical elements at the Earth and orbital elements at the Moon were collected.

3.4 Post-Launch Correction

No launch vehicle will be able to perfectly execute the desired initial conditions for the nominal trajectory, and post-launch cleanup will be required. Placement of a post-launch correction maneuver dominates the mid-course correction Δv requirements of the overall trajectory [6], making the time it is performed an important factor.

An investigation into the Δv requirements of the first maneuver with respect to time was conducted by varying the time after launch the first maneuver was placed. The initial velocity of the original trajectory was given a velocity undershoot of 10.8958 $\frac{\text{km}}{\text{s}}$ (0.0592 m/s below the nominal value) to model less than optimal launch vehicle performance. The MCS was modified to allow the first maneuver to be shifted in time between the initial state and its original timing. An analyzer profile was created to vary the timing of the maneuver placement from 60 seconds post launch to 20 days in intervals of 3 hours. The differential corrector profile was given control parameters of 3D maneuver magnitude of the first maneuver and equality constraints of position and velocity at the patch point. The timing and maneuver magnitude of the second maneuver was not changed. 3D maneuver data and time after launch were collected.

3.5 Comparison to Reduced-Fidelity Model

As mentioned previously, lower-fidelity models have been used to provide better initial guesses in higher-order models. This approach was used in works by Belbruno and Miller [4], Koon et al. [15] and Luo and Topputo [18], with the work done by Belbruno and Miller [4] utilizing a higher-order model that included planetary ephemeris, solar radiation pressure, and oblateness perturbations. The initial guess for their model was provided using a spatial four-body model, work by Yagasaki [35] further supported that inclusion of the Sun and a four-body model is necessary.

A lower-fidelity model was used to compare the initial and final conditions of the nominal trajectory. This model considered point-mass gravity for the Earth, Moon, and Sun in a fully elliptical inclined system. Because this model did not incorporate ephemeris data, the orbits of the massive bodies are analytical perfect Keplerian ellipses, creating an inclined bi-elliptical restricted four-body problem (IBERFBP) . For the purposes of this work, trajectories in the IBERFBP were propagated using a variable step size explicit Runge-Kutta method of order 5(4), with relative and absolute tolerances of 1×10^{-12}. The final state in this model was defined using the Cartesian vectors for velocity and position relative to the Moon at perilune arrival, expressed in the Earth J2000 frame. The state was then integrated backwards in time until reaching the periapsis above the Earth, with the perilune velocity being adjusted to ensure the correct Earth departure altitude. Resulting position and velocity vectors and time of flight were compared to the nominal trajectory. Using only the Moon HPOP propagator to simulate the trajectory, propagator forces were selectively removed to explore effects and consistency with the reduced-fidelity model.

The radiation pressure model within the high-fidelity model assumes the spacecraft is spherical with an area of $20\,\mathrm{m}^2$, a dry mass of $200\,\mathrm{kg}$, and a fuel mass of $106\,\mathrm{kg}$ (for a total

area-to-mass ratio of 0.0654 $\frac{\mathrm{m}^2}{\mathrm{kg}}$). The reflectivity coefficient of 1 assumes the spacecraft is a fully absorbing body (a value of 2 would note a fully reflective body). The acceleration from solar radiation pressure on the spacecraft is calculated by Equation 3.5 [9].

$$a = -\mathrm{C_r}\frac{A}{m}\frac{K\phi}{c}\left(\frac{1}{R_{AU}}\right)^2 \hat{r}_s \tag{3.5}$$

$\mathrm{C_r}$ is the coefficient of reflectivity, A is area of the spacecraft, m is the mass of the spacecraft, K is the percentage of the Sun as seen from the spacecraft that is not eclipsed, ϕ is the solar flux at 1 Astronomical Unit (AU), c is the speed of light, R_{AU} is the distance from the spacecraft to the Sun in AU, and $\hat{r}_s$ is the unit vector from the spacecraft toward the Sun.

Chapter 4

Results and Analysis

This chapter employs the methods established in Chapter 3 to demonstrate trends in the design of low energy lunar transfers. The nominal "zero-maneuver" trajectory is used as a baseline for the parametric and variational studies of departure and arrival. The original GRAIL-A trajectory is used to determine a propulsive requirement trend for the first corrective maneuver timing. The nominal trajectory is then adjusted to determine equivalent launch energies for different arrival inclinations at the Moon. Finally, the nominal trajectory is compared to an equivalent trajectory in the Inclined Bi-Elliptical Four-Body Model.

4.1 Parametric and Variational Studies of Departure and Arrival

These studies were conducted by varying each element of the orbit, either the beginning of the trajectory around the Earth or the end of the trajectory around the Moon. Each study allowed for the two midcourse maneuvers to be freely changed to patch the forward and backwards sequences together with the equality constraints and tolerances outlined in Chapter 3. These two maneuvers were held constant at the time of the two deterministic maneuvers planned for the GRAIL mission. Based on the schedule, the first mid-course correction maneuver is consistent with the GRAIL-A2 maneuver and the second mid-course

correction maneuver is consistent with the GRAIL-A3 maneuver; the maneuvers will be labelled as such for the remainder of the chapter.

4.1.1 Keplerian Elements of the Target Lunar Orbit

Each lunar arrival element was varied independently of the other Keplerian elements for the following studies. The beginning of the trajectory at the Earth remained constant for every study in this subsection. These studies assumed the same capture burn at the Moon as the original trajectory.

Inclination of Target Lunar Orbit

In this study, the inclination of the target orbit around the moon was varied from 0° to 180°, covering a full range of orbits around the Moon. Δv at each 0.5° step was recorded for both maneuvers. The total mid-course Δv of the trajectory was calculated and presented in the Figure 4.1.

It is seen that the as the orbit becomes more equatorial or increasingly retrograde, the maneuver cost becomes greater. This is expected as the nominal trajectory includes no maneuvers; however, the fuel cost of increasing past 90° is similar to the fuel cost of creating a more equatorial orbit. It can be seen that even after launch, mid-course maneuvers can achieve large inclination changes for relatively small Δv costs; in addition, because these inclination changes happen mid-course, no additional propulsion is required once capture is completed. Given that the capture burn in this scenario is 191.7 m/s, it may not be unreasonable to assume that the spacecraft can perform maneuvers with enough Δv to reach all inclinations. This will establish the 255 m/s baseline used throughout the remaining variational studies.

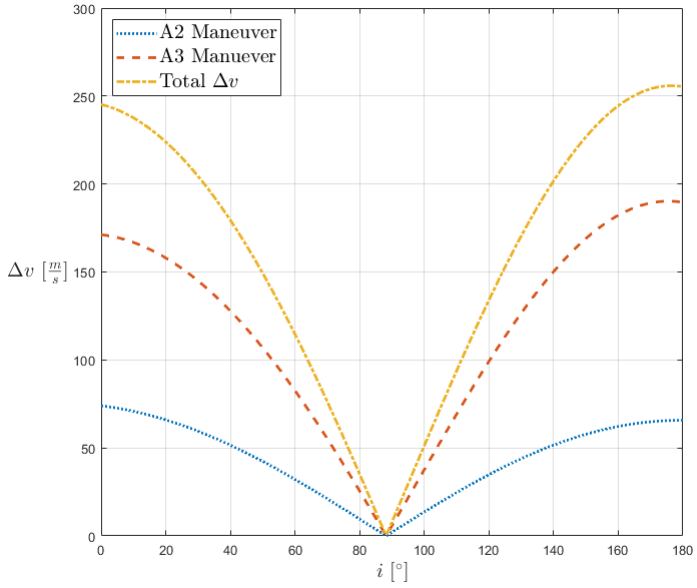

Figure 4.1: Mid-course Δv requirements for Lunar arrival orbit inclination. The blue dotted line represents the GRAIL-A2 maneuver, the red dashed line represents the GRAIL-A3 maneuver, and the yellow dash-dotted line represents the sum of these maneuvers.

Right Ascension of the Ascending Node of the Target Lunar Orbit

The right ascension of the ascending node (RAAN) was varied a full 360° in the analyzer profile. The total mid-course Δv was calculated for the entire trajectory at each 0.5° step and presented in the Figure 4.2.

Here the structure is not symmetrical because of the changes in the second mid-course maneuver (A3), its maneuver magnitude falling below that of the first maneuver before increasing dramatically, mainly a result from the maneuver cost of the second maneuver. The first maneuver increased from the nominal trajectory to a peak of 400 $\frac{\mathrm{m}}{\mathrm{s}}$. Additionally, the differential corrector was only able to successfully converge the trajectory for RAAN between 72.5° and 185.5°. Investigating angles outside of this bound showed that the trajectory would no longer leave the influence of the moon instead continuing to stay within the orbit of the

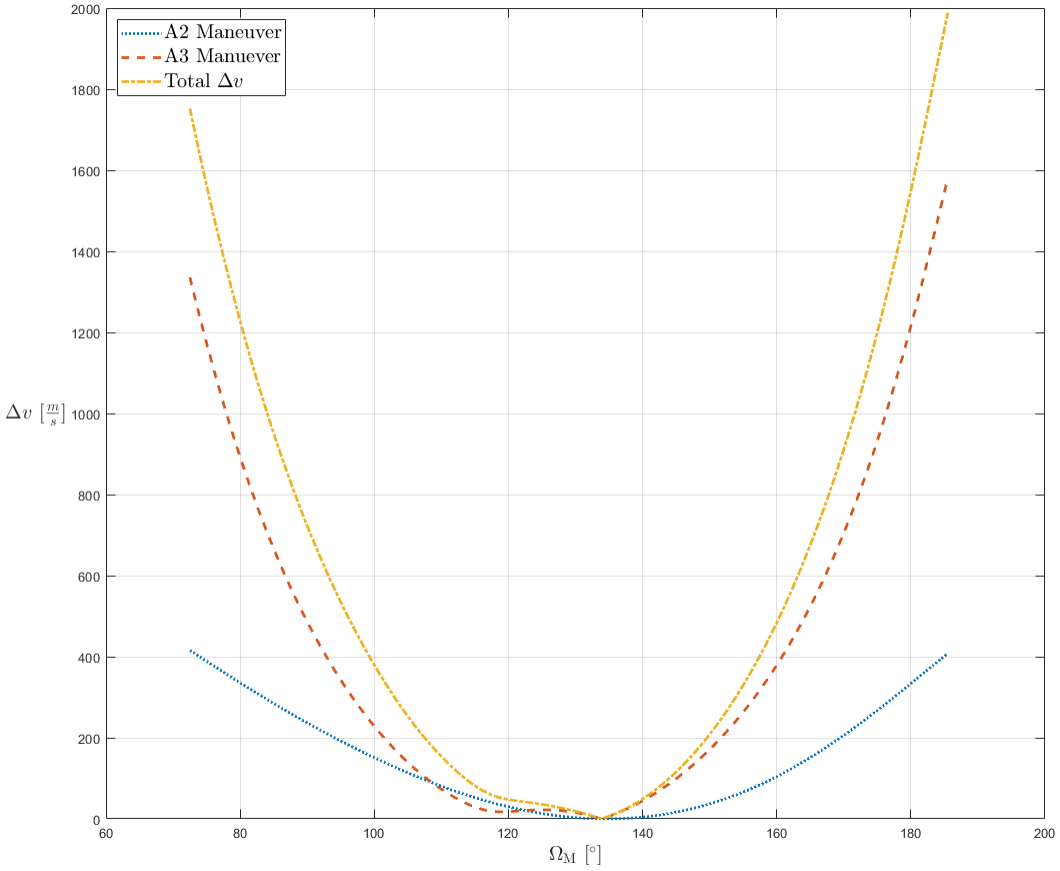

Figure 4.2: Right Ascension of the Ascending Node of the target lunar orbit. The blue dotted line represents the GRAIL-A2 maneuver, the red dashed line represents the GRAIL-A3 maneuver, and the yellow dash-dotted line represents the sum of these maneuvers.

Moon. Example trajectories outside these bounds is shown in the Figure 4.3.

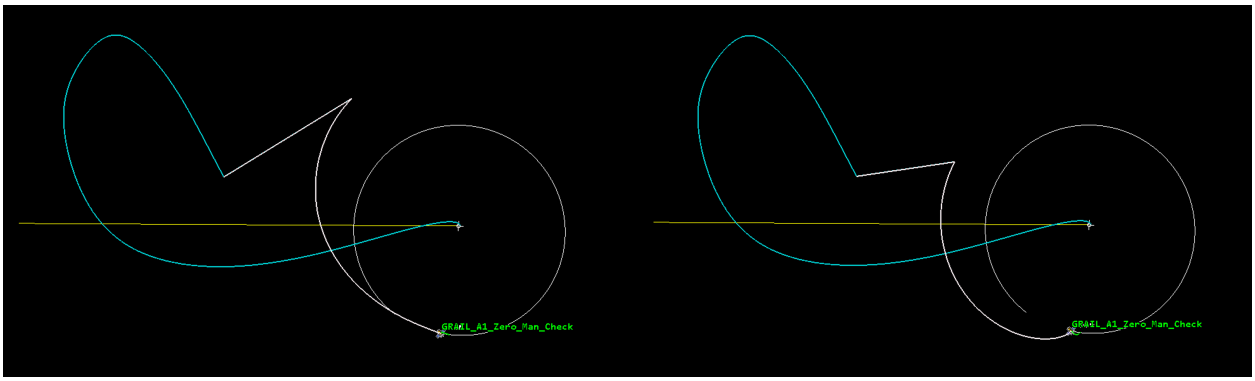

Figure 4.3: Low energy transfer with arrival orbit RAAN of 71°(left) and 186° (right). The blue trajectory is the forward propagation from the Earth, and the off-white trajectory is the backwards propagation from the Moon. The white orbit is the Moon's orbit and the yellow line is the Earth-Sun line. The straight white line connecting the blue and white trajectories is a graphical artifact within STK.

It can be seen that RAAN changes are reasonable for an approximate 40° range; considering the mid-course Δv requirements for the full range of orbit inclinations (Figure 4.1) as a baseline. Outside of this range, the mid-course Δv requirements grow dramatically, following the A3 maneuver trend. While it may be of interest to arrive into an orbit with a certain right ascension of the ascending node, it may not be as important as other elements (mainly inclination and orbit insertion epoch) and can be cheaply changed using the J2 precession.

Argument of Periapsis of the Target Lunar Orbit

The argument of periapsis of the target lunar orbit was varied from 0° to 360°, with the total Δv of each maneuver being recorded in Figure 4.4.

The differential corrector profile was able to successfully re-converge the trajectory for arguments of periapsis between 0° and 75° and between 259° and 360°. The maneuver cost exhibits a double peak within each range, resulting from the second mid-course maneuver. The first maneuver resulted in a peak magnitude of 625 $\frac{\text{m}}{\text{s}}$. Similar to the RAAN variation

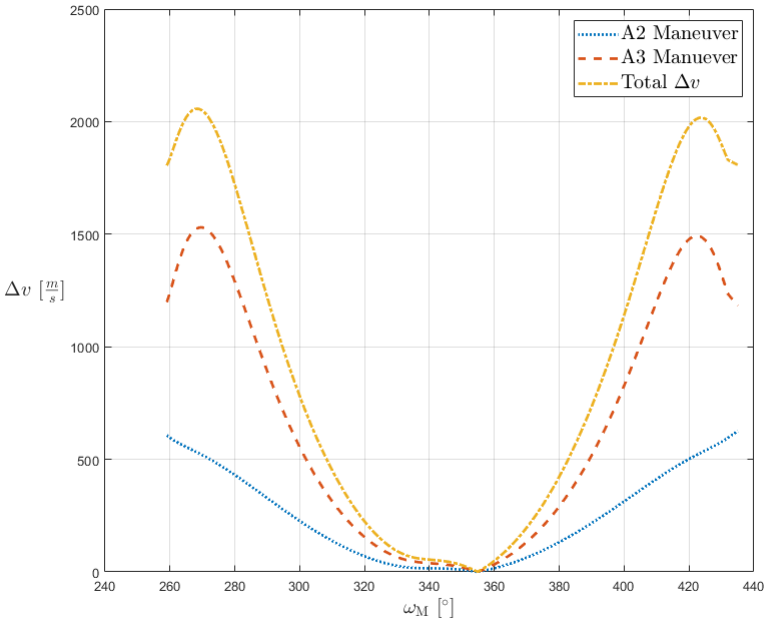

Figure 4.4: Argument of Periapsis of the target lunar orbit.The blue dotted line represents the GRAIL-A2 maneuver, the red dashed line represents the GRAIL-A3 maneuver, and the yellow dash-dotted line represents the sum of these maneuvers.

study, the corrector profile failed to converge between 75° and 259° degrees, the result of the trajectory not being able to leave the orbit of the moon. This is shown in Figure 4.5.

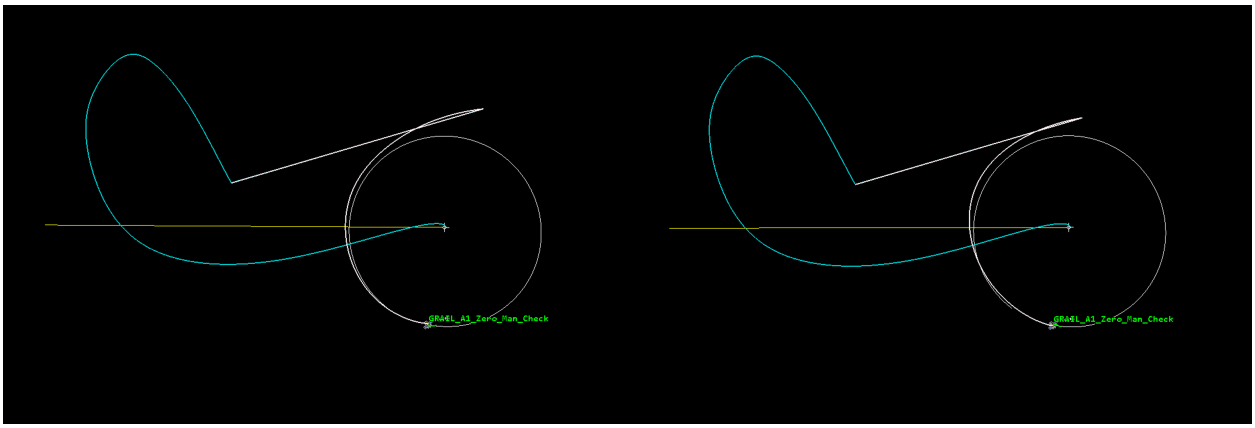

Figure 4.5: Low energy transfer with arrival orbit argument of periapsis of 76° (left) and 258° (right). The blue trajectory is the forward propagation from the Earth, and the off-white trajectory is the backwards propagation from the Moon. The white orbit is the Moon's orbit and the yellow line is the Earth-Sun line.

It can be seen that argument of periapsis changes are reasonable for an approximate 50° range, this is if the mid-course Δv requirements for the full range of orbit inclinations (Figure 4.1) is considered. Outside of this range, the mid-course Δv requirements become fuel prohibitive, following the A3 maneuver trend.

Epoch of Lunar Orbit Insertion

The lunar orbit insertion epoch, corresponding to the arrival time at the Moon, was varied $\pm$ 7 hours within the analyzer tool, and the two maneuvers were adjusted to compensate for the changed arrival time given the fixed launch epoch. The total Δv for both maneuvers was recorded and shown in Figure 4.6.

From this figure, it can be seen that the Δv requirements for arrival time vary linearly with time, with reducing the total TOF requiring more Δv than increasing the TOF. The mid-

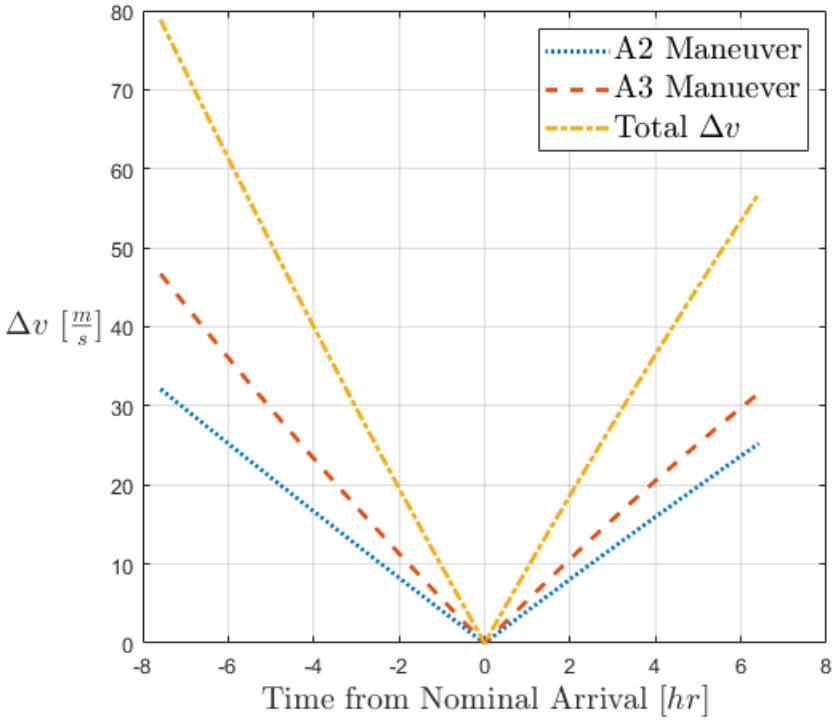

Figure 4.6: Arrival epoch of lunar orbit insertion. The blue dotted line represents the GRAIL-A2 maneuver, the red dashed line represents the GRAIL-A3 maneuver, and the yellow dash-dotted line represents the sum of these maneuvers.

course Δv requirements for these maneuvers are relatively small compared to the baseline established.

Comparison

The studies for the various lunar arrival conditions were compared to each other to evaluate propulsion requirements relative to the offset from the nominal trajectory. The results are given in Figure 4.7. The comparison between the arrival orbital elements are limited within the 255 m/s baseline established from the inclination of the lunar arrival orbit variational study. The comparison between the full range of elements studied are presented in Figure A.1 in Appendix A.

Comparatively, the most expensive elements to adjust after launch are the right ascension of the ascending node and the argument of periapsis of the arrival orbit. Outside of the converged range, changing these elements will create a trajectory that does not approach the Earth-Sun L_1 vicinity (in reverse time), and therefore it is expected to see higher propulsion requirements.

While a mission launching independently would be likely to have a trajectory designed specifically for it, any missions that utilize a ride-share system or contain multiple components would benefit from the trends apparent within the results. The reasonable changes to the elements of the arrival orbit post launch would fall under the overall maneuver baseline of 255 m/s. However, it is more likely to that adjustments to the arrival inclination or arrival epoch are more useful than RAAN and argument of periapsis, as those elements change over time of the orbit from gravitational precessions. For instance, if a future mission launched multiple satellites in a constellation, but required each satellite to go to differing orbital inclinations (e.g. 30° and 90°), the expected additional mid-course Δv required between the

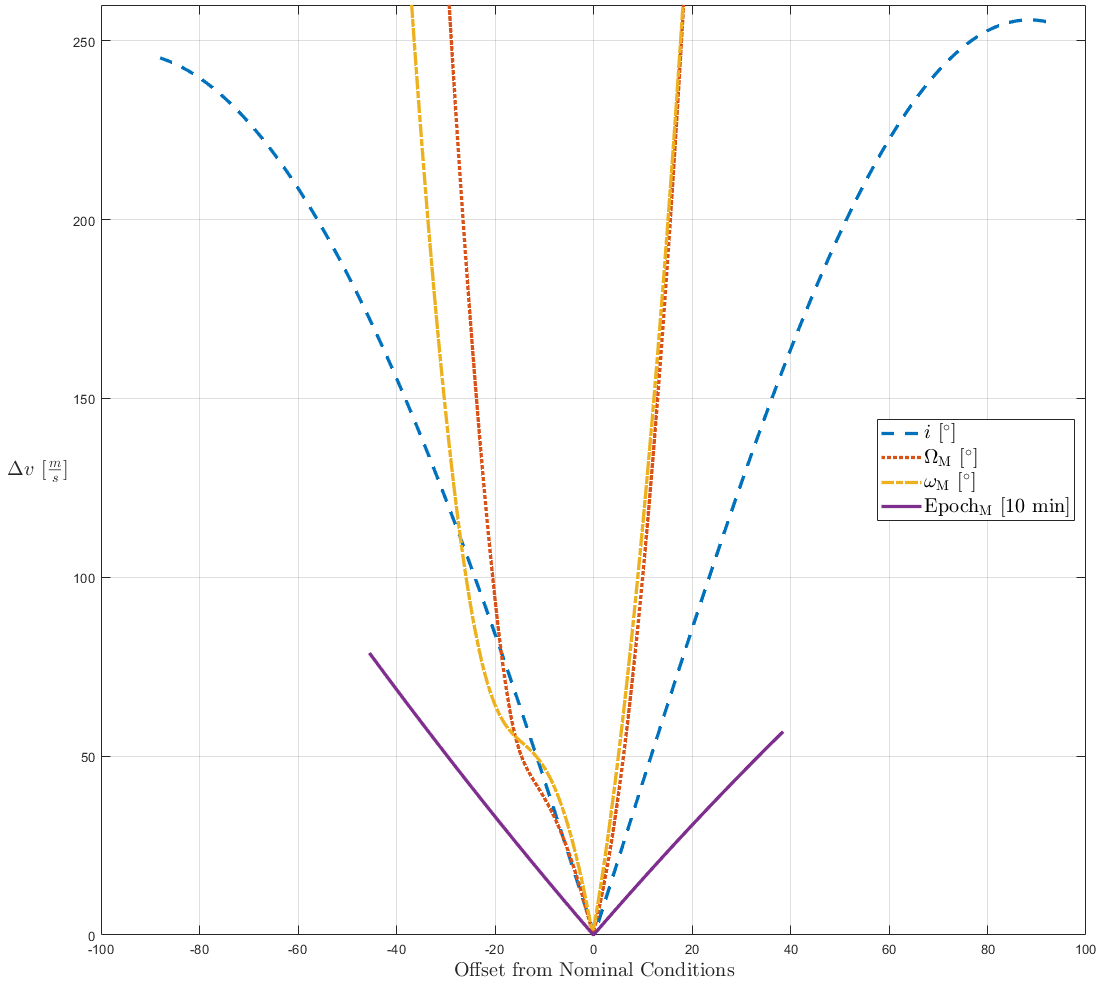

Figure 4.7: Comparison of lunar arrival conditions. The purple solid line is insertion epoch, the blue dashed line is orbit inclination, the red dotted line is RAAN, and the yellow dash-dotted line is argument of periapsis. This displays the total mid-course Δv requirement by the offset from the nominal trajectory. Units for each offset are in the legend.

two satellites would be ∼250 m/s. The second maneuver along the trajectory appears to be more heavily weighted in the adjustments for each of the lunar orbital elements; this can be seen as the second maneuver being used more to target the proper conditions. However, this could potentially be reduced by adjusting the timing of the two maneuvers; such a study would be the subject of future work.

4.1.2 Earth Elements

Each element at the Earth was varied independently of the other spherical elements. The lunar arrival conditions were kept constant. This investigation could be seen as a "return-to-nominal" method given differing off-nominal launch conditions.

Orbital Radius

Orbital radius was varied using the analyzer tool between 6671 $\frac{\text{km}}{\text{s}}$ and 6700 $\frac{\text{km}}{\text{s}}$ while keeping all other elements constant. This was to simulate launching into higher orbits with the same velocity, thus launching into higher energies.

As shown in Figure 4.8, keeping the same initial orbit velocity but placing the departure point higher from the Earth will create greater propulsion requirements for the spacecraft, mainly in the form of slowing down to reduce excess energy. Additionally, reducing the radius will create propulsion requirements to speed up the spacecraft as the initial velocity is not sufficient to provide the trajectory with enough energy.

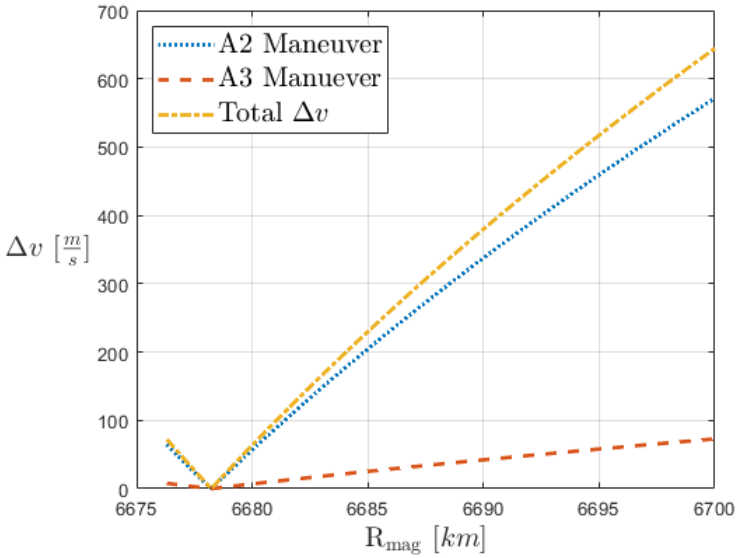

Figure 4.8: Orbit Radius of trans-lunar injection (TLI). The blue dotted line represents the GRAIL-A2 maneuver, the red dashed line represents the GRAIL-A3 maneuver, and the yellow dash-dotted line represents the sum of these maneuvers.

Orbital Velocity

Orbital velocity was varied from 10.89 $\frac{\text{km}}{\text{s}}$ to 11 $\frac{\text{km}}{\text{s}}$ using a 0.0005 $\frac{\text{km}}{\text{s}}$ step size. The total Δv for both maneuvers was recorded. The differential corrector was able to converge within equality constraints between 10.8955 $\frac{\text{km}}{\text{s}}$ and 11 $\frac{\text{km}}{\text{s}}$.

From Figure 4.9 there is a similar behavior to varying the orbital radius, as providing more initial velocity will result in a higher launch energy if the orbit radius is held constant. To counteract this, the first maneuver (A2) requires more propulsion to offset the increased launch energy while the second maneuver (A3) would supplement. The similarity between these two plots confirm the behavior is due to energy error, regardless of the source of energy error. This led to the investigation in Section 4.3.

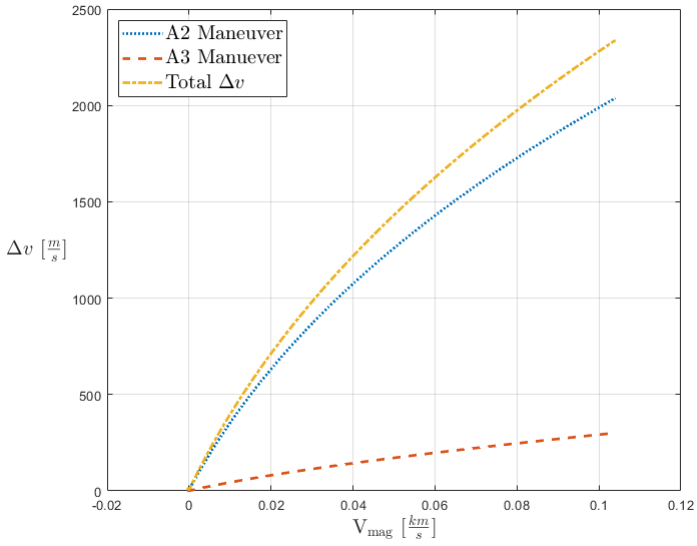

Figure 4.9: Initial orbital velocity of trans-lunar injection point. The blue dotted line represents the GRAIL-A2 maneuver, the red dashed line represents the GRAIL-A3 maneuver, and the yellow dash-dotted line represents the sum of these maneuvers

Trans-Lunar Injection Epoch

The epoch of the trans-lunar injection from Earth orbit was varied 7 hours before and after the converged nominal time. The total Δv for both maneuvers was recorded in Figure 4.10.

The differential corrector profile converged for every step size of the analyzer profile. This supports that utilizing a low energy lunar transfer allow for longer launch windows. The required mid-course Δv for varying the launch window is very small; however the shape of the maneuvers does not seem to follow any structure. Work done by Belbruno and Carrico [2] in 2000 investigated expanding the launch window under a single mid-course correction maneuver placed at apogee (1.5×10^6 km from Earth). It was found that the mid-course Δv requirement varied linearly with time from nominal launch, out to 10 min on either side of nominal launch time, reaching 40 m/s of required mid-course Δv. The results from the investigation in this thesis suggest that it is less costly to expand the launch window using

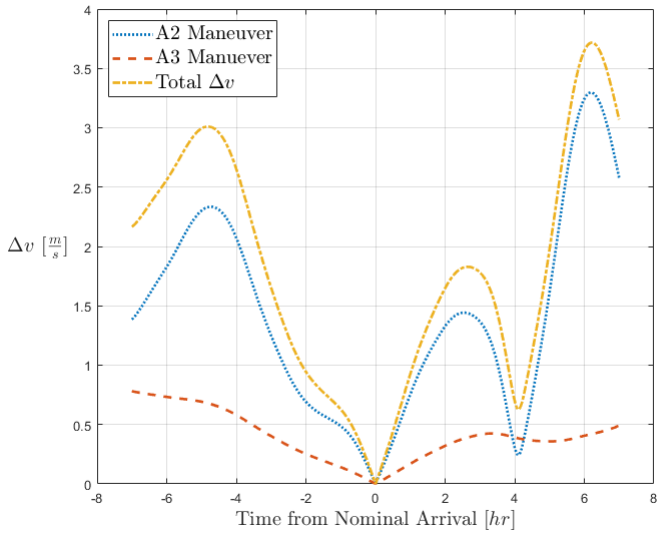

Figure 4.10: Trans-lunar injection epoch. The blue dotted line represents the GRAIL-A2 maneuver, the red dashed line represents the GRAIL-A3 maneuver, and the yellow dash-dotted line represents the sum of these maneuvers

more than one maneuver and placing them in different points along the trajectory, supporting the claim that apogee is not necessarily the optimal placement for corrective maneuvers [2].

Comparison

The Earth elements were compared to each other to evaluate propulsion requirements relative to the offset from the nominal trajectory. The results of the comparison within the 255 m/s baseline can be seen in Figure 4.11. The full range of elements in the variational study can be seen in Figure A.2 in Appendix A.

Comparatively, the most expensive elements to adjust (or, more precisely, correct for errors in), are the orbital radius and the orbital velocity, with the orbital velocity being more expensive to correct (this is from the energy offsets). These elements in their extremes will create a trajectory that would become a transit trajectory through the Earth-Sun L_1 point and enter interplanetary space. For a mission utilizing ride-share it is important that the

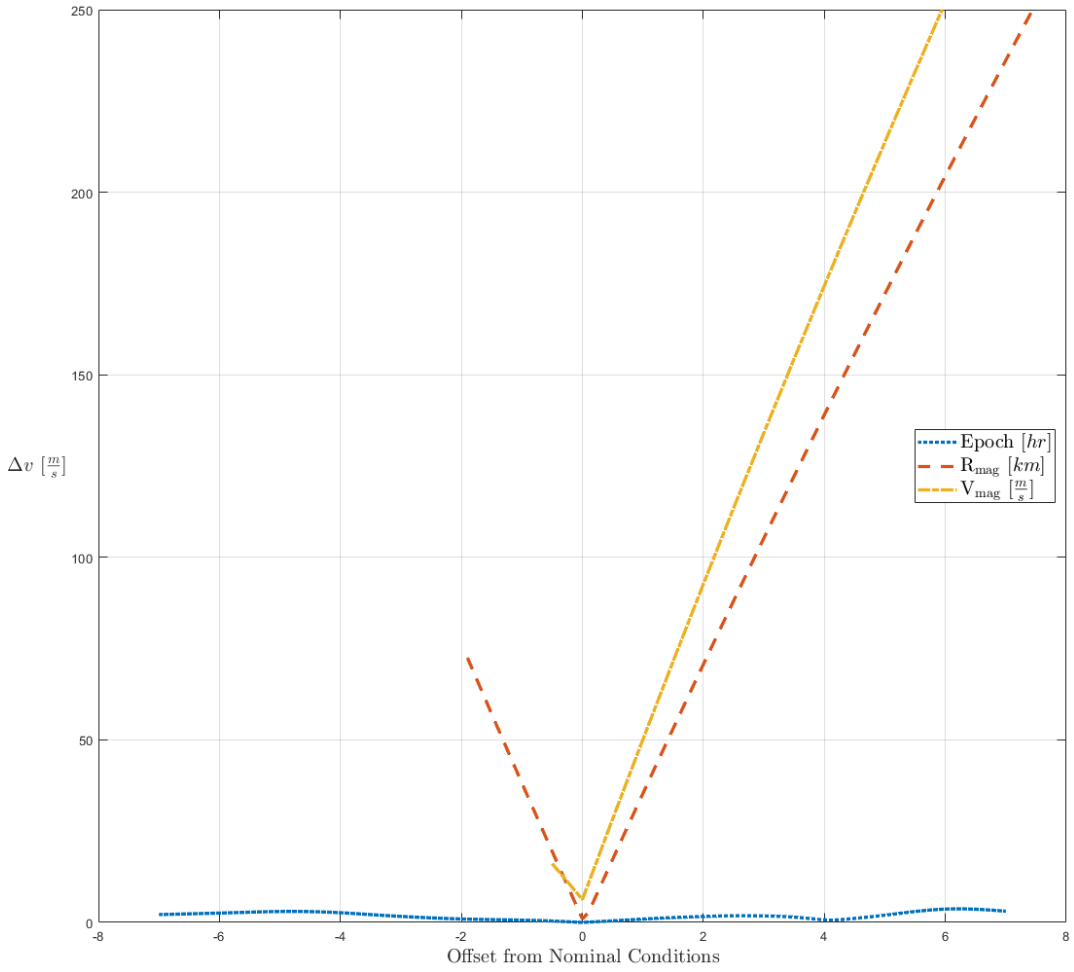

Figure 4.11: Comparison of Earth departure elements relative to their offset from the nominal trajectory. The blue dotted line is TLI epoch, the red dashed line is the initial orbital radius of the TLI point, the yellow dash-dotted line is initial velocity at TLI. Units for the offset are in the legend.

launch vehicle energy is as close to the required launch energy for the mission as possible; large deviations from the launch energy are costly to correct for. Launch vehicle considerations for ride-share would be more important than the launch time of the accompanying mission. The TLI epoch can be cheaply accounted for (requiring no more than 4 m/s of Δv to shift it by 7 hours), making this less important than the required energy.

4.2 Departure and Arrival Energies of the Nominal Trajectory

Because the target inclination for lunar arrival is the most feasible and useful variation, the required launch energy and arrival energy of a spacecraft to capture at the Moon into differing inclinations was investigated. This utilized the same differential profile to create the nominal trajectory in Chapter 3. The differential corrector profile was able to converge inclinations between 10° and 110°. The equivalent energy was calculated with equations 3.3 and 3.4 and the results of this variational study can be seen in Figures 4.12a and 4.12b.

The launch energy required at Earth remains relatively similar when compared to the energy required at the Moon; this is likely because there are a small range of energies that reach the vicinity of the Earth-Sun L_1 point but do not transit to interplanetary space. Closer inspection of Earth energy shows that it varies parabolically between $-0.325\,976\,\frac{\text{km}^2}{\text{s}^2}$ and $-0.327\,223\,\frac{\text{km}^2}{\text{s}^2}$. The required energy at the Moon almost depends linearly on the inclination, with higher inclinations arriving with higher Keplerian energy relative to the Moon. This is likely due to the out-of-plane motion required to achieve a polar orbit approach.

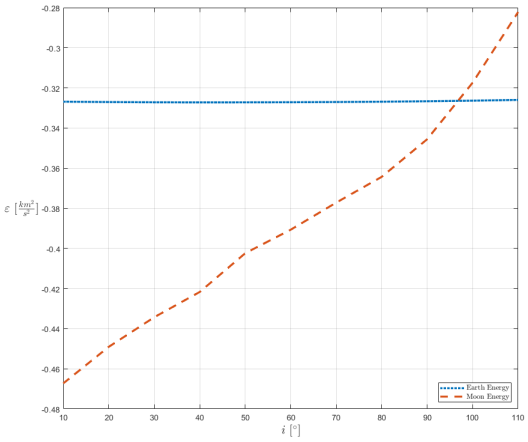

(a) Earth launch and Moon arrival energies for different arrival inclinations of the nominal trajectory. The red dashed line is Keplerian energy at the Moon and the blue dotted line is specific orbital energy at Earth.

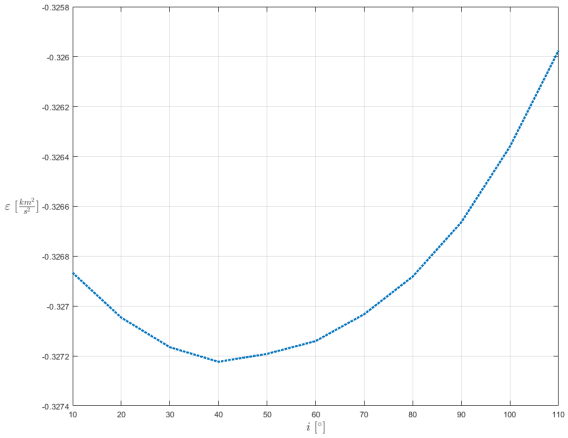

(b) Specific orbital energy for launch from Earth for different arrival inclinations at the Moon.

4.3 Timing of the Post-Launch Correction Burn

The differential corrector profile was able to converge conditions from 2 minutes post launch to up to 4.5 days within the given constraint tolerance. The required Δv per Δv_{error} was calculated as well as the equivalent Δv per $\Delta \text{R}_{\text{error}}$ using the energy equation. The results are provided in Figure 4.13.

If there is a launch error, the cost to correct the error grows quickly after the launch. This shows that increased tracking immediately after launch in beneficial to reduce the required Δv later on. For example, if the launch vehicle can guarantee a 1 m/s tolerance on velocity, and the correction burn can be no greater than 10 m/s, the correction burn must be performed no later than 2.25 days after launch. If a launch vehicle can guarantee a radius tolerance of 1 km and no more than 10 m/s can be allocated to the correction burn, it must be performed within 3.5 days.

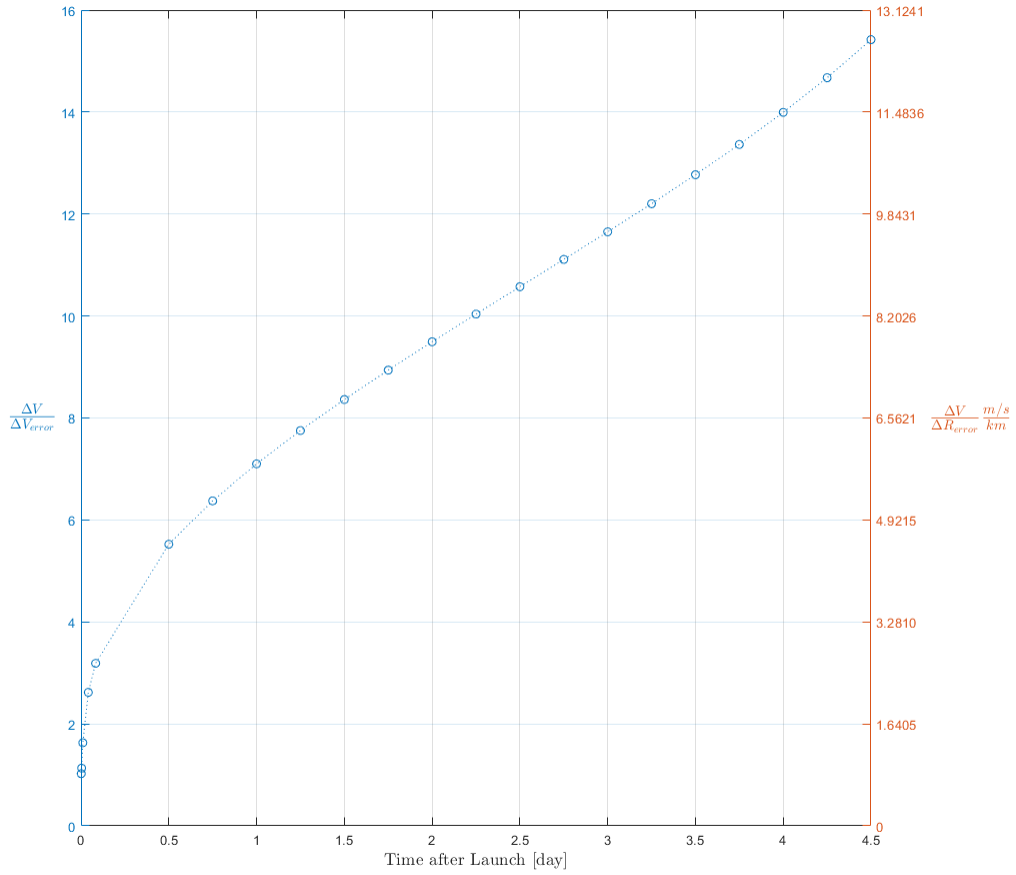

Figure 4.13: Normalized post launch correction burn. The left axis shows the required Δv per velocity error in launch. The right axis provides the equivalent Δv requirement per radius error in launch. These are related by the specific orbital energy equation.

4.4 Comparison to Reduced-Fidelity Model

Using the final vector at the Moon, the trajectory was propagated in reverse time within the IBERFBP model. The initial vectors at the Moon and time-of-flight in the IBERFBP model along with the vectors from the simulation in STK are presented in Table 4.1.

Table 4.1: Final vector comparisons between models for a nominal trajectory.

Model	Position (1000s of km)	Velocity (km/s)	TOF (days)
IBERFBP	[-1.1820, -1.3295, 0.3908]	[-0.2447, -0.8458, 2.1371]	88.5398
STK	[-1.1820, -1.3295, 0.3909]	[-0.2449, -0.8465, 2.1389]	112.3576

While the final vector conditions match closely, the TOF for the transfers does not align. Additionally, the trajectory shape within the IBERFBP shows a much smaller loop in the vicinity of the Earth-Sun L_1 point than the nominal trajectory in STK.

An adjusted trajectory to force the correct time of flight was created by providing an additional velocity at perilune arrival of 1.31 m/s, and a maneuver at the patch point (15.4409 days before arrival) with the components [-1.26112, -0.10278, 0] km/s in the ecliptic J2000 frame. These Δvs were chosen to force the IBERFBP trajectory to match the TOF and Earth departure radius of the nominal STK trajectory using the minimum Δv at the specific patch point. These results given in Table 4.2. Figure 4.14 shows the nominal and adjusted trajectories in the IBERFBP model.

Table 4.2: Final vector comparisons between models for adjusted trajectory.

Model	Position (1000s of km)	Velocity (km/s)	TOF (days)
IBERFBP	[-1.1820, -1.3295, 0.3908]	[-0.2448, -0.8462, 2.1383]	112.3576
STK	[-1.1820, -1.3295, 0.3909]	[-0.2449, -0.8465, 2.1389]	112.3576

A possible cause for the TOF discrepancy between nominal trajectories in each model could be from the inclusion of solar radiation pressure in the STK model. Creating a trajectory that

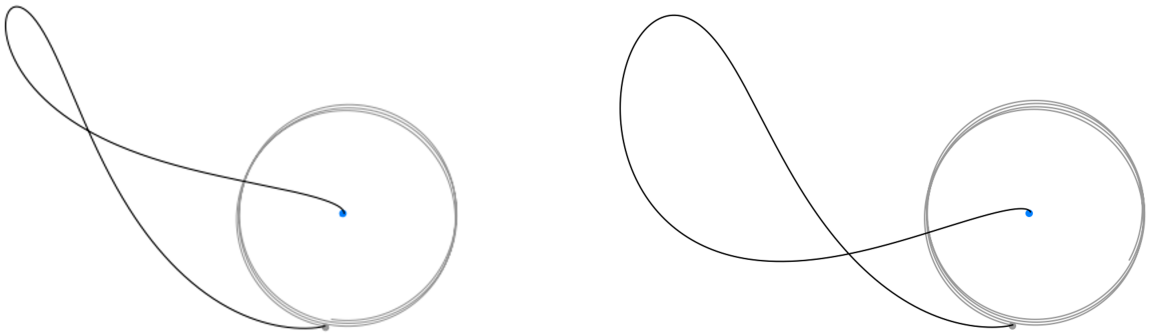

Figure 4.14: Inclined Bi-Elliptic Restricted Four Body Problem Trajectories. On the left, the unperturbed trajectory is shown; on the right, the perturbed trajectory is shown. These trajectories have similar converged conditions with different times of fligth.

propagates in reverse time from the Moon using solely the Moon HPOP Propagator (ignoring higher-order terms of the Earth gravity field), yields a trajectory with a 1 km difference in orbit radius at the departure time from Earth from the nominal trajectory. This suggests that inclusion of an Earth gravitational field model is important but not significant enough to greatly affect the trajectory. When the solar radiation pressure propagator function is excluded, the backwards trajectory no longer reaches the Earth; instead, reaching just to the orbit of the Moon returning from vicinity of the Earth-Sun L_1 point at the end of the trajectory duration.

The point of periapsis now occurs on September 8 2011 10:47:22.738 UTCG (adding 2.1338 days to the 112.3576 day TOF of the nominal trajectory); and the TLI radius occurs at 1680.4 m rather than the nominal 300.2 m (a 1380.2 m difference).

Given that the total magnitude of the adjustments made to the nominal trajectory in the IBERFBP model sum to 2.575 m/s, the total effect of solar radiation pressure could be the cause. The resulting trajectories with these propagator omissions are in Figure 4.15. It is therefore recommended that any future studies of low-energy transfers include the effects of

SRP, especially where the timing of the transfers is important.

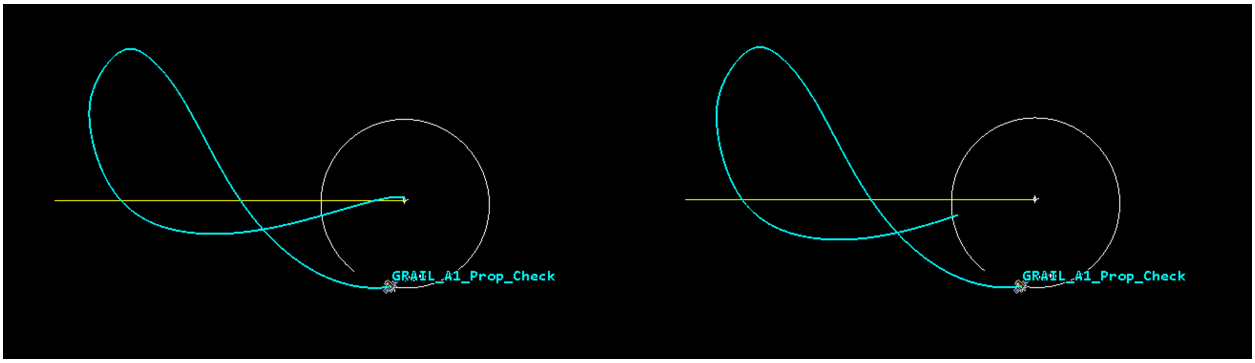

Figure 4.15: Truncated models of the dynamics in the four-body system based on the STK Moon HPOP v10 propagator. On the left, the propagator included the spherical harmonic model of the lunar gravity field, point mass approximations for the Earth and Sun, and solar radiation pressure. The trajectory on the right further omits solar radiation pressure. The blue trajectory is the backwards propagated transfer from the Moon, the yellow line is the Earth-Sun line, and the white orbit is the orbit of the Moon.

Chapter 5

Conclusion

Given renewed interest to return to the Moon and establish a permanent presence, exploration of more efficient ways to achieve lunar orbit are required. Low energy lunar transfers are one way to achieve this; by leveraging the gravitational effects of multiple bodies these transfers require lower propulsion requirements than similar Hohmann transfers [4, 30, 35]. Due to their chaotic nature, small adjustments along these trajectories can result in large changes upon arrival, albeit with more tracking requirements necessary and much longer transit times.

5.1 Main Findings

Simulating low energy lunar energy transfers within STK allowed for a more dynamically accurate representation of the Earth-Sun-Moon system than simplified models like the circular restricted three-body problem (CRTBP) and the Inclined Bi-Elliptic Restricted Four Body Problem (IBERFBP). The standard definitions and propagators within Astrogator allow for easier higher-fidelity simulations utilizing planetary ephemeris data and spherical harmonic gravity field models. The GRAIL-A trajectory was recreated using a patched forward-backward sequence, the backward sequence depending on the Moon HPOP propagator and the forward sequence relying on the Earth HPOP Propagator. From this original trajectory, a nominal "zero-maneuver" trajectory was created by varying Earth departure

and lunar arrival conditions to eliminate to mid-course maneuvers performed by the GRAIL mission. Variational studies utilized the nominal trajectory to determine propulsion requirements for changing lunar conditions and correcting for different launch conditions.

It was found that lunar arrival conditions can be easily adjusted utilizing the two mid-course correction maneuver structure applied in the GRAIL mission, although right ascension of the ascending node and argument of periapsis require drastically increased requirements (when compared to lunar orbit insertion epoch and target orbit inclination) due to the trajectory failing to approach the Earth-Sun L_1 point in reverse-time departure from the moon. Varying lunar arrival inclination required no more than 255 m/s of mid-course Δv for both prograde and retrograde equatorial orbits from a nearly polar orbit. Right ascension of the ascending node could be reasonably reached within a 40° range from nominal, and argument of periapsis could be reasonably reached within a 50° range. Lunar orbit insertion could be varied by 7 hours on either side of nominal arrival. These trends could be applied to determine trajectories for missions that utilize multiple parts that could go to different orbits around the Moon or expand ride-share options.

Varying the orbital radius, initial orbital velocity, and epoch at Earth showed that the most expensive elements to correct from are orbital velocity and radius. The orbit epoch investigation supported the claim that low-energy lunar transfers create larger launch opportunities, consistent with Lehman et al. [17] and Kim et al. [14].

Equivalent energy requirements for capturing into different inclination orbits around the Moon was investigated. While the launch energy at Earth stayed relatively constant, lunar energy varied positively with lunar arrival inclination.

The timing of the first maneuver following post-launch underperformance was investigated to create a relationship between both velocity underperformance and radius underperformance.

It was found that velocity errors were much more expensive to correct than radius, and that placement of first maneuver dominated correction Δv requirements [6].

The nominal trajectory modeled in STK was compared to the a recreation of the nominal trajectory in the Inclined Bi-Elliptic Four-Body Problem. While final vector conditions matched closely, the time of flight and the shape of the trajectory deviated significantly. By adding small maneuvers at perilune and the patch point, totaling 2.575 m/s, the TOF and trajectory shape were similar. Removing propogator functions in STK revealed that solar radiation pressure played a significant role in perturbing the trajectory, especially when compared to point-mass approximations of the Earth.

5.2 Limitations

For these investigations, the maneuver timing for both of the mid-course maneuvers was held constant (except the study on post launch correction burns). While this structure did support increased launch windows and reduced correction requirements over a single maneuver at apogee, it makes no assumption that the placement of these in time is the best. Additionally, the lunar orbit insertion burn was assumed to be constant and no efforts were made to reduce the magnitude of the burn within the time frame of the GRAIL mission. Only one trajectory type was considered in this study, a highly polar orbit, which may not be entirely applicable to other orbit types (different arrival conditions), although missions following a similar type may find the qualitative findings useful.

While STK offers high-fidelity simulations, the full extent of its capabilities was not explored in this investigation. The default HPOP propagators do not include the gravitational forces from other celestial bodies nor do they include spherical gravitational field models outside of the central body; building a custom propagator that incorporates more of the propagator

functions that could be utilized at both the Earth and Moon would eliminate using more than one propagator. Additionally, the Moon HPOP propagator uses a spherical model based on the Lunar Prospector mission, a mission that was flown in 1998, where more accurate lunar gravity models now exist, such as models based on NASA GRAIL data. Ephemerides of central bodies in STK are based on the DE430 model, a model released in 2013. Currently, the most accurate model is DE440; given that STK can use custom ephemeris files, it could be implemented in the future.

5.3 Future Work

A clear continuation of this work would be to implement a more complete and accurate force propagator for trajectory estimation. As the area these trajectories follow exist within a near force-balance state, more accurate models for the forces acting on the spacecraft would be beneficial. More developed models than the ones used in this study, for planetary ephemeris and lunar gravitational fields, are available. Additionally, adding in the remaining massive bodies of the solar system, i.e. the planets, would only increase the dynamic accuracy. The role of solar radiation pressure is understated in many of the previous works on these trajectories. From comparing trajectories in the IBERFBP to the one modeled in STK, solar radiation pressure was found to provide a small but significant change to the trajectory over time.

Furthermore, investigating different maneuver placements would be beneficial to fully characterizing mid-course Δv requirements, and even further reduce lunar orbit insertion requirements. To expand on this, a catalogue of orbits with different arrival requirements could be made in higher-fidelity.

5.4 Summary

Low energy lunar transfers offer a more efficient pathway to the Moon over traditional methods. While the time-of-flight for these transfers is greatly increased, comparatively; the chaotic nature of these transfers can be leveraged to ease propulsion requirements for mission success. They are able to reach a wide range of lunar arrival conditions for lower Δv cost, thus enabling lower cost missions and increasing the payload that can be carried to the Moon. With these transfers, establishment of lunar infrastructure and human presence among the stars becomes more a economically realizable goal.

Bibliography

[1] E. BELBRUNO. Lunar capture orbits, a method of constructing earth moon trajectories and the lunar gas mission. In *19th International Electric Propulsion Conference*, 1987. doi: 10.2514/6.1987-1054. URL https://arc.aiaa.org/doi/abs/10.2514/6.1987-1054.

[2] Edward Belbruno and John Carrico. Calculation of weak stability boundary ballistic lunar transfer trajectories, 2000. URL https://arc.aiaa.org/doi/abs/10.2514/6.2000-4142.

[3] Edward Belbruno, Marian Gidea, and Francesco Topputo. Weak stability boundary and invariant manifolds. *SIAM J. Applied Dynamical Systems*, 9:1061–1089, 2010. doi: 10.1137/090780638.

[4] Edward A. Belbruno and James K. Miller. Sun-perturbed earth-to-moon transfers with ballistic capture. *Journal of Guidance, Control, and Dynamics*, 16(4):770–775, 1993. doi: 10.2514/3.21079. URL https://doi.org/10.2514/3.21079.

[5] C. C. Conley. Low energy transit orbits in the restricted three-body problem. *SIAM Journal on Applied Mathematics*, 16(4):732–746, 1968. ISSN 00361399. URL http://www.jstor.org/stable/2099124.

[6] Riley M Fitzgerald. *Optimization and Characterization of Chance-Constrained Guidance, Navigation, and Control for Low-Energy Lunar Transfers*. Dissertation, Massachusetts Institute of Technology, 2021.

[7] William M. Folkner, J. G. Williams, Dale H. Boggs, Ryan S. Park, and Petr Kuchynka. The planetary and lunar ephemerides de430 and de431. 2014.

[8] F. García and G. Gómez. A note on weak stability boundaries. *Celestial Mechanics and Dynamical Astronomy*, 97(2):87–100, 2007. ISSN 1572-9478. doi: 10.1007/s10569-006-9053-6. URL https://doi.org/10.1007/s10569-006-9053-6.

[9] Analytical Graphics, Dec 2022. URL https://help.agi.com/stk/12.5.0/index.htm#gator/eq-solar.htm.

[10] Gerard Gómez, Wang Sang Koon, Martin W. Lo, Jerrold E. Marsden, Josep J. Masdemont, and Shane D. Ross. Connecting orbits and invariant manifolds in the spatial restricted three-body problem. *Nonlinearity*, 17:1571–1606, 2004.

[11] Sara Hatch, Min-kun Chung, Julie Kangas, Stacia Long, Ralph Roncoli, and Theodore Sweetser. Trans-lunar cruise trajectory design of grail (gravity recovery and interior laboratory) mission. In *AIAA/AAS Astrodynamics Specialist Conference*, 2010. doi: 10.2514/6.2010-8384. URL https://arc.aiaa.org/doi/abs/10.2514/6.2010-8384.

[12] Nicola Hyeraci and Francesco Topputo. The role of true anomaly in ballistic capture. *Celestial Mechanics and Dynamical Astronomy*, 116(2):175–193, 2013. ISSN 0923-2958. doi: 10.1007/s10569-013-9481-z. URL https://dx.doi.org/10.1007/s10569-013-9481-z.

[13] L. G. Jacchia. Thermospheric Temperature, Density, and Composition: New Models. *SAO Special Report*, 375, March 1977.

[14] Young-Rok Kim, Young-Joo Song, Jae-Ik Park, Donghun Lee, Jonghee Bae, Seungbum Hong, Dae-Kwan Kim, and Sang-Ryool Lee. Orbit determination simulation

for korea pathfinder lunar orbiter using ballistic lunar transfer. In *AAS/AIAA Astrodynamics Specialist Conference, 2020, August 9, 2020 - August 12, 2020*, volume 175 of *Advances in the Astronautical Sciences*, pages 3147–3162. Univelt Inc., 2020. ISBN 00653438. Compilation and indexing terms, Copyright 2022 Elsevier Inc. 20221111794795 Aerospace research Exploration projects Lunar orbit insertions Lunar orbiter Lunar transfers Orbit determination Orbit prediction Research institutes Trajectory correction manoeuvres Trans Lunar trajectories.

[15] W. S. Koon, M. W. Lo, J. E. Marsden, and S. D. Ross. Low energy transfer to the moon. *Celestial Mechanics and Dynamical Astronomy*, 81(1):63–73, 2001. ISSN 1572-9478. doi: 10.1023/A:1013359120468. URL https://doi.org/10.1023/A:1013359120468.

[16] Wang Sang Koon, Martin W. Lo, Jerrold E. Marsden, and Shane D. Ross. *Dynamical Systems, the Three-Body Problem and Space Mission Design*. Marsden Books, 2011. ISBN 978-0-615-24095-4.

[17] David H. Lehman, Tom L. Hoffman, and Glen G. Havens. The gravity recovery and interior laboratory mission. In *2013 IEEE Aerospace Conference, AERO 2013, March 2, 2013 - March 9, 2013*, IEEE Aerospace Conference Proceedings. IEEE Computer Society, 2013. ISBN 1095323X. doi: 10.1109/AERO.2013.6496866. URL http://dx.doi.org/10.1109/AERO.2013.6496866. Compilation and indexing terms, Copyright 2022 Elsevier Inc. 20132416416356 Gravitational fields Gravity Recovery and Climate Experiment missions Internal structure Jet Propulsion Laboratory Mars reconnaissance orbiter missions Mission operations Multi-mission operations Thermal evolution.

[18] Z. F. Luo and F. Topputo. Analysis of ballistic capture in sun–planet models. *Advances in Space Research*, 56(6):1030–1041, 2015. ISSN 0273-1177. doi: 10.1016/j.asr.2015.05.042. URL https://dx.doi.org/10.1016/j.asr.2015.05.042.

[19] Z. F. Luo, F. Topputo, F. Bernelli-Zazzera, and G. J. Tang. Constructing ballistic capture orbits in the real solar system model. *Celestial Mechanics and Dynamical Astronomy*, 120(4):433–450, 2014. ISSN 0923-2958. doi: 10.1007/s10569-014-9580-5. URL https://dx.doi.org/10.1007/s10569-014-9580-5.

[20] J. J. Masdemont. High-order expansions of invariant manifolds of libration point orbits with applications to mission design. *Dynamical Systems*, 20(1):59–113, 2005. ISSN 1468-9367. doi: 10.1080/14689360412331304291. URL https://dx.doi.org/10.1080/14689360412331304291.

[21] E. Mazarico, F. G. Lemoine, Shin-Chan Han, and D. E. Smith. Glgm-3: A degree-150 lunar gravity model from the historical tracking data of nasa moon orbiters. *Journal of Geophysical Research: Planets*, 115(E5), 2010. doi: https://doi.org/10.1029/2009JE003472. URL https://agupubs.onlinelibrary.wiley.com/doi/abs/10.1029/2009JE003472.

[22] D Milligan, D Gestal, P Pardo-Voss, O Camino, D Estublier, and C Koppel. Smart-1 electric propulsion operational experience. In *Proceedings of the 29th International Electric Propulsion Conference*, page 16, 2005.

[23] K. NOCK, G. ASTON, R. SALAZAR, and P. STELLA. Lunar get away special (gas) spacecraft. In *19th International Electric Propulsion Conference*, 1987. doi: 10.2514/6.1987-1051. URL https://arc.aiaa.org/doi/abs/10.2514/6.1987-1051.

[24] Ryan S. Park, William M. Folkner, James G. Williams, and Dale H. Boggs. The jpl planetary and lunar ephemerides de440 and de441. *The Astronomical Journal*, 161(3):105, feb 2021. doi: 10.3847/1538-3881/abd414. URL https://dx.doi.org/10.3847/1538-3881/abd414.

[25] Jeffrey S. Parker, Rodney L. Anderson, and Andrew Peterson. Surveying ballistic transfers to low lunar orbit. *Journal of Guidance, Control, and Dynamics*, 36(5):1501–1511, 2013. doi: 10.2514/1.55661. URL https://doi.org/10.2514/1.55661.

[26] Nikolaos K. Pavlis, Simon A. Holmes, Steve C. Kenyon, and John K. Factor. The development and evaluation of the earth gravitational model 2008 (egm2008). *Journal of Geophysical Research: Solid Earth*, 117(B4), 2012. doi: https://doi.org/10.1029/2011JB008916. URL https://agupubs.onlinelibrary.wiley.com/doi/abs/10.1029/2011JB008916.

[27] Daniele Romagnoli and Christian Circi. Earth–moon weak stability boundaries in the restricted three and four body problem. *Celestial Mechanics and Dynamical Astronomy*, 103(1):79–103, 2009. ISSN 0923-2958. doi: 10.1007/s10569-008-9169-y. URL https://dx.doi.org/10.1007/s10569-008-9169-y.

[28] Ralph Roncoli and Kenneth Fujii. Mission design overview for the gravity recovery and interior laboratory (grail) mission. In *AIAA/AAS Astrodynamics Specialist Conference*, 2010. doi: 10.2514/6.2010-8383. URL https://arc.aiaa.org/doi/abs/10.2514/6.2010-8383.

[29] Stephen Scheuerle Jr. *Construction of Ballistic Lunar Transfers in the Earth-Moon-Sun System*. Thesis, Purdue University, 2021.

[30] Priscilla Sousa-Silva, Maisa O. Terra, and Matteo Ceriotti. Fast earth–moon transfers with ballistic capture. *Astrophysics and Space Science*, 363(10):210, 2018. ISSN 1572-946X. doi: 10.1007/s10509-018-3431-x. URL https://doi.org/10.1007/s10509-018-3431-x.

[31] VICTOR Szebehely. Chapter 1 - description of the restricted problem. In VICTOR Szebehely, editor, *Theory of Orbit*, pages 7–41. Academic Press, 1967. ISBN 978-0-

12-395732-0. doi: https://doi.org/10.1016/B978-0-12-395732-0.50007-6. URL https://www.sciencedirect.com/science/article/pii/B9780123957320500076.

[32] Michael Thompson, Ethan Kayser, Jeffrey Parker, Connor Ott, Matthew Bolliger, Thomas Gardner, and Bradley Cheetham. Navigation design of the capstone mission near nrho insertion. In *AAS/AIAA Space Flight Mechanics Meeting*, 08 2021.

[33] F. Topputo and E. Belbruno. Earth–mars transfers with ballistic capture. *Celestial Mechanics and Dynamical Astronomy*, 121(4):329–346, 2015. ISSN 1572-9478. doi: 10.1007/s10569-015-9605-8. URL https://doi.org/10.1007/s10569-015-9605-8.

[34] Francesco Topputo. On optimal two-impulse earth–moon transfers in a four-body model. *Celestial Mechanics and Dynamical Astronomy*, 117(3):279–313, 2013. ISSN 0923-2958. doi: 10.1007/s10569-013-9513-8. URL https://dx.doi.org/10.1007/s10569-013-9513-8.

[35] Kazuyuki Yagasaki. Sun-perturbed earth-to-moon transfers with low energy and moderate flight time. *Celestial Mechanics and Dynamical Astronomy*, 90(3-4):197–212, 2004. ISSN 0923-2958. doi: 10.1007/s10569-004-0406-8. URL https://dx.doi.org/10.1007/s10569-004-0406-8.

[36] Tung-Han You, Peter Antreasian, Stephen Broschart, Kevin Criddle, Earl Higa, David Jefferson, Eunice Lau, Swati Mohan, Mark Ryne, and Mason Keck. Gravity recovery and interior laboratory mission (grail) orbit determination. 2012.

[37] Maria T. Zuber, David E. Smith, David H. Lehman, Tom L. Hoffman, Sami W. Asmar, and Michael M. Watkins. *Gravity recovery and interior laboratory (GRAIL): Mapping the lunar interior from crust to core*, volume 9781461495840 of *GRAIL: Mapping the Moon's Interior*, pages 3–24. Springer New York, 2014. doi: 10.1007/

978-1-4614-9584-0_2. URL http://dx.doi.org/10.1007/978-1-4614-9584-0_2. Compilation and indexing terms, Copyright 2022 Elsevier Inc. 20194507650362 Lunar Lunar gravity field Middle school students Ranging systems Science objectives Science operations Terrestrial planets Thermal evolution.

Appendices

Appendix A

Variational Studies Elements Comparison

The figures presented within this appendix are the comparisons for the full range of elements conducted during the variational studies. Figure A.1 contains the variations of every element of the lunar arrival orbit; this is the complete set of data presented in Figure 4.7. Figure A.2 contains the variations of every element of the TLI point at Earth; this contains the complete set of data presented in Figure 4.11.

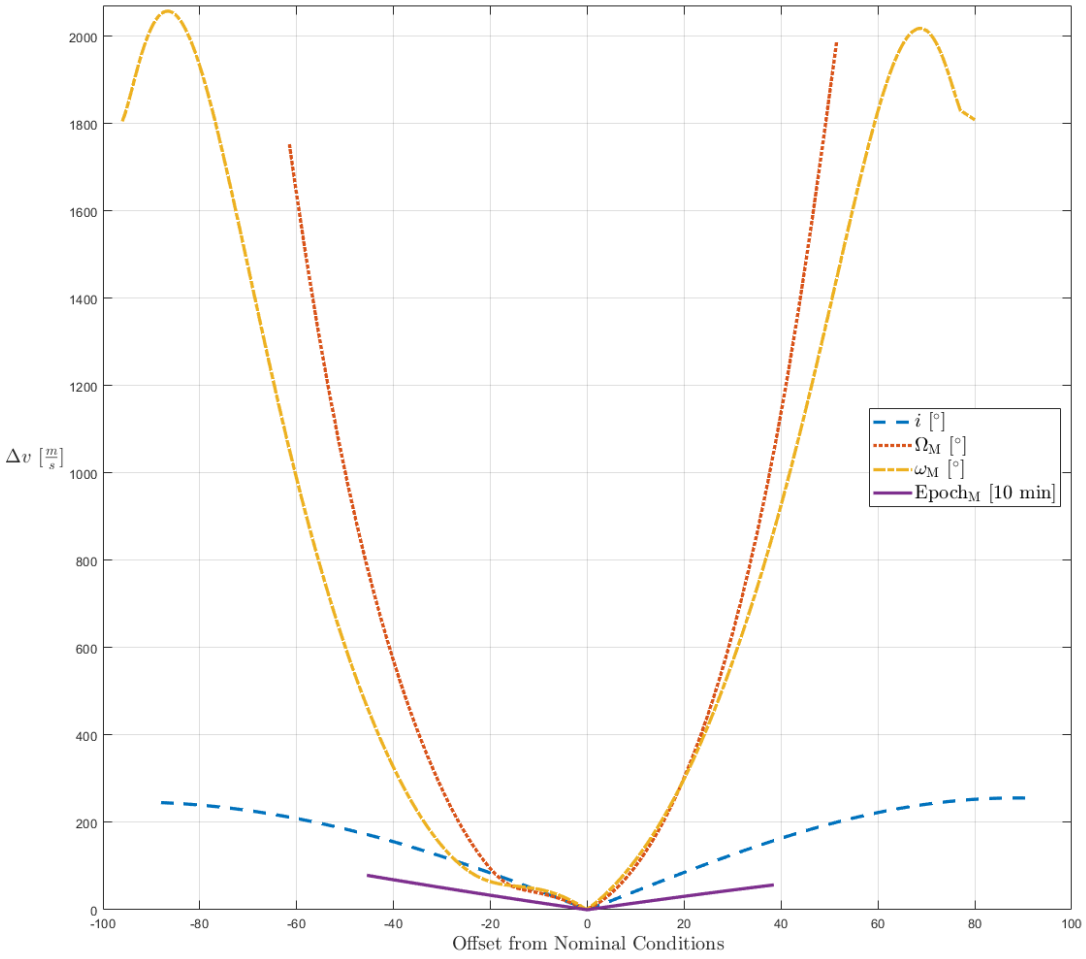

Figure A.1: Comparison of lunar arrival conditions. The purple solid line is insertion epoch, the blue dashed line is orbit inclination, the red dotted line is RAAN, and the yellow dash-dotted line is argument of periapsis. This displays the total mid-course Δv requirement by the offset from the nominal trajectory. Units for each offset are in the legend.

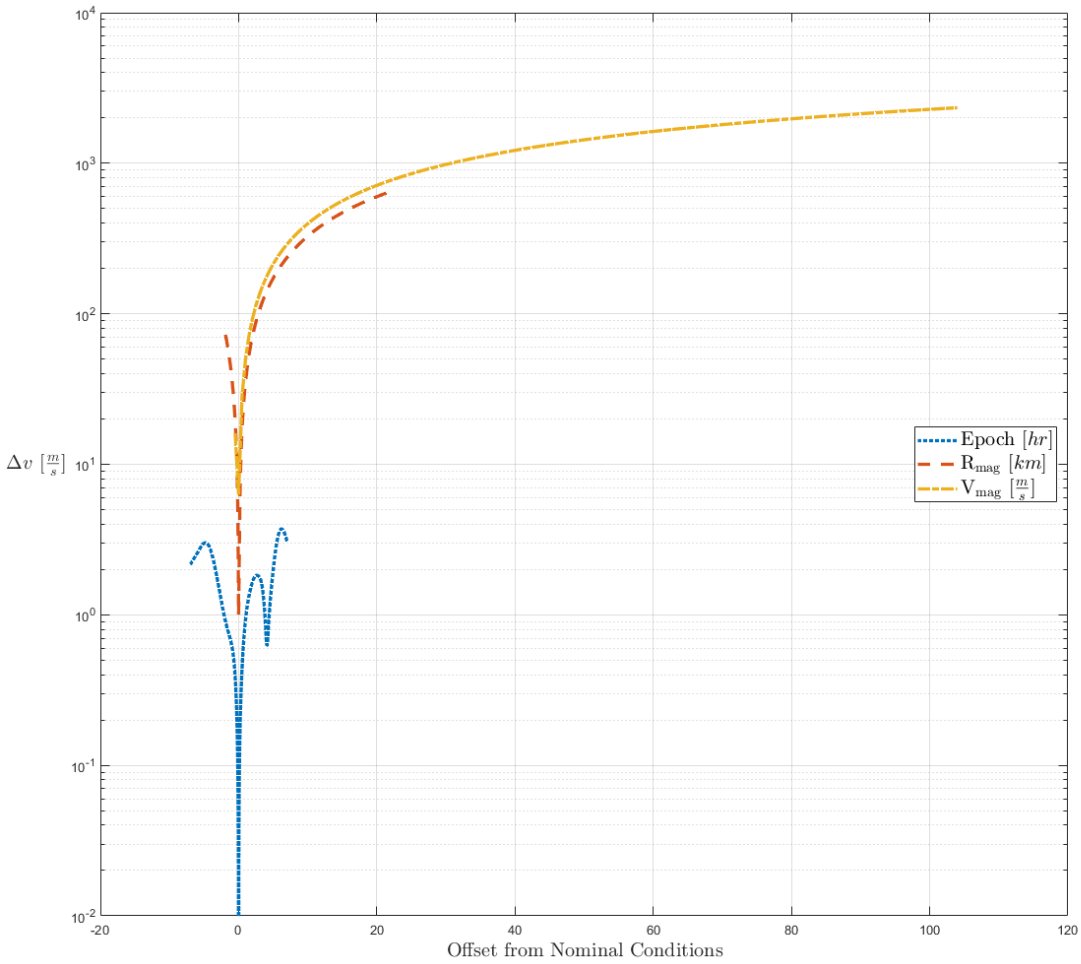

Figure A.2: Comparison of Earth departure elements relative to their offset from the nominal trajectory on a semilog plot with logarithmic y axis. The blue dotted line is TLI epoch, the red dashed line is the initial orbital radius of the TLI point, the yellow dash-dotted line is initial velocity at TLI. Units for the offset are in the legend.